Coastal Engineering 184 (2023) 104342

Contents lists available at ScienceDirect

Coastal Engineering

journal homepage: www.elsevier.com/locate/coastaleng

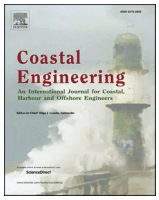

2DH modelling and mapping of surfbeat-driven flooding in the shadow of a jettied tidal inlet

Alphonse Nahon [a,*], André B. Fortunato [a], Filipa S.B.F. Oliveira [a], Alberto Azevedo [a], Maria João Henriques [a], Paulo A. Silva [b], Paulo Baptista [b], Paula Freire [a]

[a] National Laboratory for Civil Engineering, Lisbon, Portugal
[b] Centre for Environmental and Marine Studies, University of Aveiro, Aveiro, Portugal

ARTICLE INFO

Keywords:
Overtopping
Intermediate beach
Ebb-tidal delta
Infragravity waves
XBeach

ABSTRACT

Near estuaries and harbours, submerged shoals and defence structures impact the exposure to overtopping. These features may be accounted for in two-dimensional horizontal (2DH) numerical models, either based on phase-resolving or phase-average solvers for wave propagation. In between, surfbeat solvers, such as in XBeach, combine an affordable computational cost with the ability to generate and propagate the longer infragravity (IG) waves. However, surfzone wave characteristics and the overtopping exposure modelled with XBeach are sensitive to settings such as the shape of the forcing wave spectra and the numerical scheme for wave propagation. The present paper explores this sensitivity and assesses the performance of different inundation models built with the 2DH surfbeat solver of XBeach. These models were forced with downscaled water levels and directional wave spectra and the results fuelled a discussion bounded by data collected downdrift of the entrance to the harbour of Figueira da Foz (Portugal). The original second-order upwind scheme, which propagates short-waves with a lower numerical diffusion improved the model performance in terms of long-wave height, and an unconventional breaking criterion better represented the cross-shore distribution of short-wave height near the shore. A calibrated model was validated through the hindcast of an overtopping event observed under moderate swell forcing, and was used to map the overtopping exposure during a hypothetical combination of an energetic swell with a water level having a return period of ~70 years. Compared to the default wave spectra shape and model settings, using an appropriate representation of the short-wave directional spectrum at the open boundary was necessary to reproduce the observed overtopping extent. Refining the cross-shore resolution of the model helped to better represent the observed inundation extents, as also did the reduction of the friction coefficient. Additional phase-resolving simulations in 1DH overestimated IG wave energy and produced higher and more frequent overtopping discharges. The differences with the calibrated 2DH surfbeat model increased with the proximity of the inlet and with short-wave height and angle of incidence. Overall, required calibration steps were provided. They aim at making 2DH XBeach surfbeat a credible tool for 1) predicting short and IG wave characteristics up to the shoreline, as well as for 2) providing first estimates of exposure to overtopping in areas with shallow and alongshore-irregular morphologies.

1. Introduction

Increasing exposure to overtopping worldwide (Almar et al., 2021; Vitousek et al., 2017) has fostered the development of tools for simulating and mapping the contribution of wind-generated waves to present and future marine flooding hazards (Chaumillon et al., 2017; Nicolae Lerma et al., 2018; Vousdoukas et al., 2016). Methods for mapping marine flooding range from the computationally efficient static approaches (Breilh et al., 2013; Gallien, 2016), to fully dynamic approaches that use demanding numerical solvers of processes up to the wave-by-wave contributions (e.g., Le Roy et al., 2015). In between, accounting for estimates of overflowing volumes was shown to reduce the overprediction of flooded areas in the static approaches (i.e., semi-dynamic approaches described in Breilh et al., 2013), and wave overtopping discharges have been accounted for in high-resolution inundation models as source points (e.g., Smith et al., 2012). In such

* Corresponding author.
E-mail address: anahon@lnec.pt (A. Nahon).

https://doi.org/10.1016/j.coastaleng.2023.104342
Received 7 November 2022; Received in revised form 22 April 2023; Accepted 26 May 2023
Available online 27 May 2023

cases, discharges should be computed with empirical formulas (e.g., EurOtop 2018), or with process-based wave solvers, usually applied in one horizontal dimension (1DH) and at discrete cross-shore transects (e.g., Gallien 2016; Nicolae Lerma et al., 2018; Saulnier et al., 2020). Still, these approaches may miss hydro- and geomorphological features like nearby inlet jets, breakwaters, sandbanks and irregular foreshores. These features influence the propagation of short wind-waves, with periods below 25 s, and the generation/amplification of their longer period counterparts associated with short-wave groups, i.e., infragravity waves. Hereafter referred to as IG waves, infragravity waves have periods of up to 4 min (see Bertin et al., 2018, for a review). In the surfzone of dissipative and intermediate beaches or across tidal flats, they may become the dominant source of sea surface height variability as the short wind-waves dissipate (Gent, 2001; Raubenheimer and Guza, 1996).

To better account for such hydro- and geomorphological variability, models must represent the two horizontal dimensions (2DH). For instance, to propagate wind waves across irregular fringing coral reefs, Quataert et al. (2020) and Leijnse et al. (2021) used a phase-resolving solver (XBeach, non-hydrostatic; hereafter XB-NH) in 2DH. For comparison, Quataert et al. (2020) also applied the surfbeat solver of XBeach (hereafter XB-SB), and analysed their models distinguishing up to the very low frequency motions (4-to-30 min periods). Overall, they found a good agreement across the reef platform, the main difference being higher wave runup levels at the shoreline with XB-NH. In their Philippine example, Leijnse et al. (2021) also used XB-NH to force the marine boundary of a reduced-physics inundation model. In both cases, the 2DH models based on XB-NH account for wave refraction and diffraction over the irregular and channelized fringing reefs, unlike a 1DH model would do (Storlazzi et al., 2022). However, phase-resolving applications require more important computing resources due to the higher spatio-temporal resolution needed compared to phase-average ones.

Therefore, in addition to the 1DH *vs.* 2DH question, the debate between a phase-resolving and a phase-average approach is legitimate. Indeed, before the study of Quataert et al. (2020), Lashley et al. (2018) reported that, at least when applied in 1DH, phase-resolving models may underperform phase-average models in terms of the wave-induced setup. Hence, methodologies to estimate the total water level along irregular coastlines may still benefit from phase-average models applied in 2DH. These models are particularly beneficial in areas where the foreshore has an irregular and shallow morphology. In such places, IG waves can play a major role in the inundation process and should therefore be well accounted for (Lashley et al., 2020; van Ormondt et al., 2021). The surfbeat mode of XBeach was developed to account for these processes and has been proven to perform on par with empirical formulas in predicting storm impacts at a partially engineered beach (de Santiago et al., 2017). Also, because in 2DH the surfbeat solver accounts for the effect of directional wave spreading, XBeach performs better than in 1DH (either in surfbeat or phase-resolving modes) in terms of modelled wave runup at reflective beaches (Roelvink et al., 2018), only slightly underestimating observed runup. Therefore, local applications of XB-SB are expected to model overtopping accurately for a wide range of coastal morphologies. However, Roelvink et al. (2018) stressed that the performance of XB-SB strongly depends on the representation of the wave groupiness, which in XB-SB is affected by the numerical solver for short-wave propagation and by the characteristics of the short-wave directional spectrum imposed at the offshore boundary.

To improve XB-SB's stability, Roelvink et al. (2018) proposed to increase the numerical diffusion (i.e., *warmbeam* default option) while simultaneously modifying the way directionally-spread short-waves are propagated (i.e., *single-dir* option). Still, studies with the original second-order upwind scheme (e.g., Bertin and Olabarrieta 2016; Lashley et al., 2019) performed well, provided that appropriate directional wave spectra were used at the model's offshore boundary. Indeed, the energy and runup of IG waves are tightly linked to the spectral spreading in both direction and frequency (Guza and Feddersen, 2012; Van Dongeren et al., 2003), and, independently of the numerical scheme used, the best agreements with hydrodynamic and/or run-up data were produced by forcing offshore boundaries with observed or downscaled directional wave spectra (Bertin et al., 2020; Bertin and Olabarrieta, 2016; de Beer et al., 2021; Lashley et al., 2019; Mouragues et al., 2021; Stockdon et al., 2014). Hence, accounting for the spectral characteristics of the wave field is expected to be an essential aspect of overtopping predictions.

Under the above considerations, the spreading of XBeach as an operational tool in coastal engineering pauses the question of how much cunning is required to push it further and improve our ability to predict of coastal flooding. This study helps answering this question by developing a methodology to estimate coastal overtopping and to create maps of flooded areas with XB-SB. The methodology was applied to the waterfront of Cova-Gala, which is located on the central western coast of Portugal. This beach extends to the south of the commercial harbour of Figueira da Foz and is partially engineered with rocky groins and seawalls. The following section presents these geomorphological characteristics, the dataset used to validate the local hydrodynamic model and the implementation of XBeach. **Section 3** summarises the model validation and the results of the sensitivity tests, following to which, **section 4** defines the methodology to map at-risk areas and presents the impact of the successive modelling choices on the modelled exposure to overtopping. Finally, the discussion and conclusions sections emphasise how those results should improve practices for mapping hazards associated with overtopping.

2. Data and methods

2.1. Study area

The beach of Cova-Gala is located on the central west coast of Portugal (C.-G., Fig. 1a). It is a partially engineered beach that extends 2 km southward from the southern jetty of the harbour of Figueira da Foz (Fig. 1b). The harbour lies inside the Mondego River estuary, where mesotidal tides (average and maximum tidal ranges of about 2.2 and 3.6 m, respectively) drive between 6 and 24 $\times$ 10^6 m^3 of water in and out of the estuary twice a day (Mendes et al., 2021). Combined with an average daily river flow of 6 $\times$ 10^6 m^3 (based on SNIRH, 2021), tidal exchanges maintain a large and dynamic ebb-tidal delta (Fernández-Fernández et al., 2019). This delta dampens the high waves approaching Cova-Gala.

Indeed, the western coast of Portugal has an energetic wave climate, and presents large interannual and seasonal variations. At offshore locations like the Leixões buoy (Fig. 1a, L.; used for validating the regional wave model in Appendix A.), the storm threshold for the significant (short-)wave height ($H_{S,SW}$) is defined at 4.5 m, which is in good agreement with commonly used metrics (Mendes and Oliveira, 2021). Within the Leixões buoy record between 1996 and 2015, Oliveira et al. (2018) identified 167 events during which this threshold was exceeded for more than six consecutive hours. The maximum value of $H_{S,SW}$ was then 9.2 m, the mean wave direction of 302°N and the most frequent values of short-wave directional spreading (DSPR) ranged from 10 to 25°. Those storms occurred mainly from October to April, and the average/median values of the significant wave height, the wave peak period (T_P), and the wave mean direction are respectively 2.15/1.78 m, 11.6/11.4 s, and 299.5/301.2°N.

On average, the wave regime generates a southward littoral drift estimated at 1 x 10^6 m^3/year of sand (Oliveira, 2016; Oliveira et al., 2016). In the 1960s, the construction of jetties on both sides of the estuary mouth interrupted the littoral drift, and, despite the sizeable ebb-tidal delta, Cova-Gala suffered from erosion (Rebêlo and Nave, 2022). To protect its waterfront against erosion and flooding, a combined groin field, dune and seawall defence scheme was built in the following decade. In 2008–2010 the northern jetty was extended by 400 m, further fostering the accumulation of sand updrift the river mouth, and the erosion of the downdrift Cova-Gala beach. The erosion has motivated the use of the dredged sediments from the harbour's access

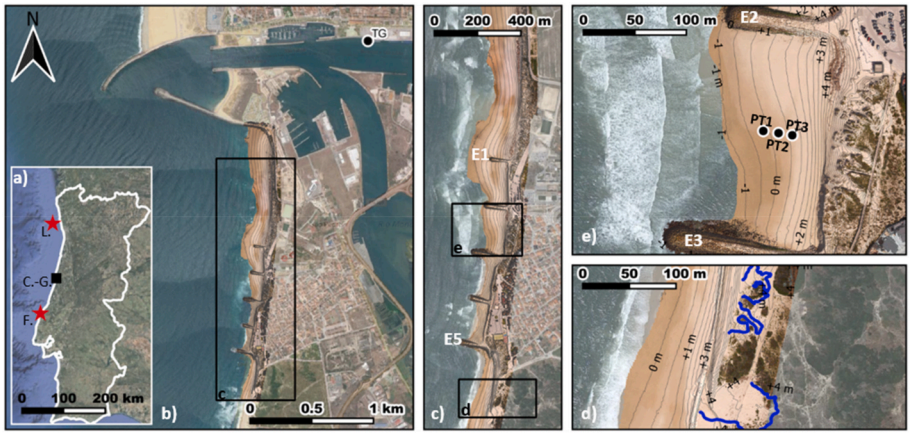

Fig. 1. Study area. **a)** Location of Cova-Gala (C.-G.) along the western coast of Portugal, of the Ferrel meteorological station (F.), and of the Leixões wave buoy (L.; background image: Google Maps); **b)** aerial view of the entrance of the Figueira da Foz harbour and of its southern margin, "TG" indicates the position of Instituto Hidrográfico's (IH) tidal gauge; **c)** Cova-Gala waterfront (background: orthophoto from 11 March 2020); **d)** in blue, overtopping extent surveyed on 21 February 2019, with topographic contours from 11 March 2020 (vertical datum: ALTH38); **e)** sandy beach cell between groins E2 e E3, instrumented with pressure transducers (PT1-3) on 10 March 2020.

channel for regular nearshore nourishments, as a complementary beach protection measure (Oliveira, 2022). The sediments are being deposited in front of the groin field within four to 10 m water depth relative to the mean sea level (MSL). Additionally, south of the 5th and southernmost groin (E5, Fig. 1c), the frontal sand dune was reinforced after a geotextile tube revetment was installed at its base in 2019.

2.2. In-situ data

2.2.1. Data acquisition

Hydro- and geomorphological data were collected at Cova-Gala in February 2019 (Freire et al., 2019) and March 2020 (Nahon et al., 2020). The datasets were used to validate the local XBeach models introduced in the next Section 2.3.1. They include a photogrammetric survey carried out on 11 February 2019 that was used as topographic input to simulate an overtopping event. This event was observed and surveyed on 21 February 2019 with a GNSS receiver in RTK mode (Fig. 1d). The hydrodynamic data include a water surface elevation record collected on 10 March 2020 by an array of pressure transducers (PT1-3, Fig. 1e). Together with a GNSS-RTK survey from the same day, this record was used to calibrate the short and IG waves in the models. The following section provides details on the PTs' data processing.

2.2.2. Hydrodynamic data processing

Data from the intertidal PTs aimed at characterising the short-wave dissipation rate, as well as estimating the height and the mean period of IG waves. The pressure data sampled at 2 Hz were converted into sea surface elevation data using the hydrostatic formula. The power spectral density (PSD) of the surface elevation records was analysed over 30-min intervals. Welch's method was employed, i.e., fast Fourier transforms (FFT) were performed over six 8.5-min segments for every interval, with a 50% overlay between consecutive segments; prior to each FFT, a Hann window was applied to every detrended segment. For every interval, the PSD (m^2/Hz) was computed as the average of all six FFTs outcomes. Next to the mean water level (MWL) curves measured at PT1 and PT3, Fig. 2 shows the PSD in decibels (i.e., 10 $log_{10}(PSD)$), computed at high tide (15h25) and for the three PTs, for frequencies between ~0.002 Hz and 1 Hz and with a resolution below 0.002 Hz. At location PT1, three peaks are present at frequencies near 0.010 Hz, 0.043 Hz and 0.075 Hz, while only the two extreme peaks were present at the other two locations.

The mean parameters for the short- and IG wave components were computed for the three locations, setting the split frequency at 0.04 Hz. This value is slightly higher than the commonly used half the short-wave peak frequency, but it already splits the middle peak at PT1 (Fig. 2). Next, the mean wave parameters were estimated from the integrated spectral moments (**Eq. (1)**), with $(f_{min}, f_{max}) = (0.04, 1)$ *Hz* for the short-wave component, hereafter denoted by subscript *SW*, and with $(f_{min}, f_{max}) = (0.001, 0.04)$ *Hz* for the IG wave component, hereafter denoted by subscript *IG*. For each component, the significant wave height (H_{m0}) and the mean period (T_{m02}) were respectively computed as **Eq. (2)** and **Eq. (3)**. In the case of the short-wave component, a non-hydrostatic correction factor (linear formula in space described by Mouragues et al., 2019) was applied to SPD after having computed the wavenumber associated with every frequency with an iterative method.

$$m_i = \int_{f_{min}}^{f_{max}} E(f) \bullet f^i \, df \qquad \text{Eq. 1}$$

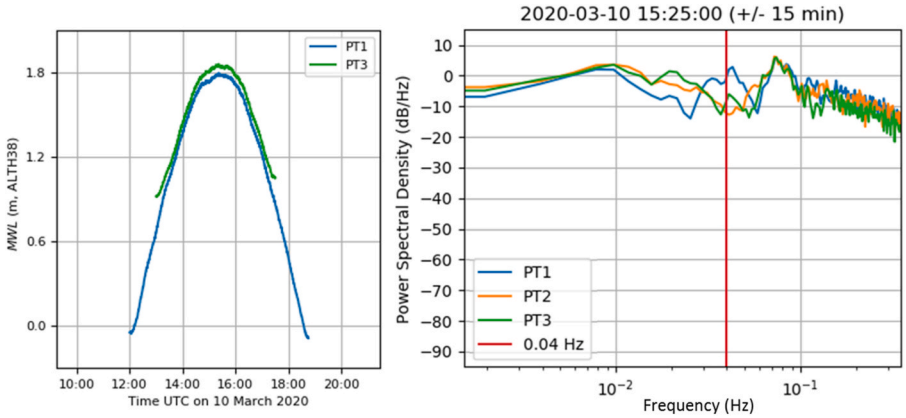

Fig. 2. Left: mean water level measured at PT1 and PT3; right: elevation power spectral density at locations PT1-3 (Fig. 1e), computed high tide on 10 March 2020.

$$H_{m0} = 4 \cdot m_0 \quad \text{Eq. 2}$$

$$T_{m02} = \sqrt{m_0 / m_2} \quad \text{Eq. 3}$$

2.3. XBeach models

2.3.1. XBeach surfbeat

The local model should be numerically efficient and capable of mapping overtopping-driven flooding while accounting for features such as tidal deltas, harbour breakwaters and coastal groins (Fig. 1). It was therefore built based on the 2DH surfbeat solver of XBeach (XB-SB; Roelvink et al., 2009; version 1.23.5527, XBeachX BETA release). Like other phase-average solvers, XB-SB solves the wave action (A) balance equation (**Eq. 4**; Holthuijsen et al., 1989), although it solves it on the relatively shorter temporal scale of the short-wave groups. However, XB-SB considers a single relative wave frequency (σ) and does not account for the advection of wave action in the frequency space, leaving the term in brackets equal to zero in **Eq. (4)**. So, in its original form, XB-SB propagates the wave action only in the horizontal plane (x, y) and in the directional space (θ). More recently, Roelvink et al. (2018) introduced the *single-dir* option, which offers a more efficient treatment of the advection in the directional space.

$$\frac{\partial A}{\partial t} + \frac{\partial c_x A}{\partial x} + \frac{\partial c_y A}{\partial y} + \frac{\partial c_\theta A}{\partial \theta} \left(+ \frac{\partial c_\sigma A}{\partial \sigma} \right) = \frac{S}{\sigma} \quad \text{Eq. 4}$$

In the present study, the source term S in **Eq. (4)** only included the dissipation by breaking ($-D_w$), unlike the generation - propagation solvers used for creating the boundary conditions (WW3 and WWM, see Appendix A.), for which the source term includes short-wave generation by the local wind. The extended expression of Roelvink (1993) was used for D_w, which is given in **Eq. (5)**, where α is a constant equal to one by default, T_{rep} is the single representative wave frequency used by XB-SB, Q_b is the fraction of wave breaking, E_w is the instantaneous integrated short-wave energy and H the associated root-mean-square wave height, and h is the instantaneous water depth.

$$D_w = 2 \frac{\alpha}{T_{rep}} Q_b E_w \frac{H}{h} \quad \text{Eq. 5}$$

Here, Q_b was computed according to Daly et al. (2012): the short-wave starts to fully break (i.e., $Q_b = 1$) once H exceeds H_{max} and only stop breaking (i.e., $Q_b = 0$) after H becomes lower than H_{reform}. Conventionally, H_{max} and H_{reform} are defined as fractions of the water depth ($\gamma \times h$) with default values of the breaking criterion ($\gamma_{def.}$) of 0.52 and 0.3, respectively. Resorting to **Eq. (6)**, XBeach further allows adding a fraction (δ) of the short-wave height to the water depth. In this rather unconventional manner, the ratio of both H_{max} and H_{reform} to h varies in time. This option was tested while adjusting the values of the breaking criterion ($\gamma_{adj.}$) as described by **Eq. (7)**.

$$H_{max/reform} = \gamma_{adj.} \times (h + \delta H) \quad \text{Eq. 6}$$

$$\gamma_{adj.} = \gamma_{def.} \; / \; (1 + \delta \gamma_{def.}) \quad \text{Eq. 7}$$

2.3.2. 2DH and 1DH cases

The model area is shown in Fig. 3. It extends from north of the entrance to Figueira da Foz harbour to the southern extremity of Cova-Gala's groin field. Westward, the area starts in ~15-m water depth (ALTH38, i.e., Cascais 1938 vertical datum), while to the east, the model domain is composed of a ~4.5 km^2 schematic back-barrier lagoon. The lagoon's dimension was based on the tidal prism-inlet cross-sectional area relationship, with Jarrett's (1976) coefficients for jettied inlets, meaning that the inlet cross-section was computed from the bathymetric data and inversely converted into the spring tidal prism with the relationship. The 3 × 4.5 km^2 domain was initially discretized with a rectilinear grid of 199 x 399 cells. Grid cells have a uniform alongshore resolution of 15 m. In the cross-shore direction, the resolution varies from 15 m to 6.5 m, being the refined area centred on the intertidal beaches and dunes/seawalls on the ocean side of the downdrift barrier-spit. With this original resolution, three model configurations were defined and are summarized in Table 1 (2D-WR, 2D-UP and 2D-LR, standing respectively for "*warmbeam*", "*upwind_2*" and calibrated "*low resolution*").

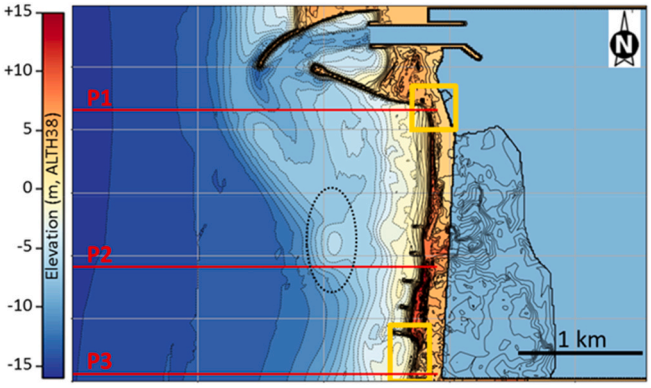

Fig. 3. - 2DH model bathymetry (March 2020) and location of the three profiles P1–P3 (in red); contour lines within the schematized lagoon represent the topographic extension used for the inundation simulations; the southern and northern yellow boxes show the location and extension of the maps on Figs. 7–8 and Fig. 10 respectively; and the dotted black line highlights the deposited dredged material.

The original 2DH configurations were complemented first with three 1DH surfbeat configurations (1D-LR, -MR, –HR respectively for "*low*", "*medium*" and "*high resolution*" in Table 1). The three configurations were run along the central profile P2 (Fig. 3), aligned with the pressure transducers, while the cross-shore grid spacing was successively divided by one, two and four. Following these sensitivity tests to the resolution, the original resolution of the 2DH models was increased by a dividing the cross-shore grid spacing by two (2D-MR and 2D-15; Table 1), like in 1D-MR. Lastly, for assessing the possible shortcomings of the 2DH surfbeat approach, in terms of the modelled wave-induced set-up and set-down, in terms of the shape of the frequency spectrum of the modelled free-surface elevations, and in terms of the modelled overtopping rates, the non-hydrostatic (NH) solver of XBeach (Roelvink et al., 2018) was employed along the three cross-shore profiles shown in red on Fig. 3. This analysis was done with the 1D-NH configuration (Table 1) and its cross-shore grid spacing divided by sixteen compared to the original resolution.

Table 1
– Model configurations according to: XBeach solver, cross-shore resolution, numerical scheme for short-wave propagation, parameters used to define H_{max} according to **Eq. (6)**, and ultimately the Manning coefficient ***n***.

Config. ID	Solver	X-shore res. (m)	scheme	δ - γ	n ($m^{-1/3}$ s)
2D-WR ([1])	2DH XB-SB	15.0–6.5	warmbeam	0.0–0.52 [1](**0.5–0.41**)	0.019
2D-UP	"	"	**upwind_2**	0.0–0.52	"
2D-LR	"	"	"	**0.5–0.41**	"
1D-LR	1DH XB-SB	"	"	"	"
1D-MR	"	7.5–3.3	"	"	"
1D-HR	"	3.8–1.6	"	"	"
2D-MR	2DH XB-SB	**7.5–3.3**	"	"	"
2D-15	"	"	"	"	**0.015**
1D-NH	1DH XB-NH	0.9–0.4	–	–	0.019

2.3.3. 1DH and 2DH model set up

Following Smit et al. (2013), the cross-shore non-hydrostatic (1D-NH) model was run with the maximum wave steepness and the wave steepness criterion to reform after breaking, respectively set equal to 0.6 and 0.3. For the surfbeat configurations, in 1DH and 2DH, the model parameters were defined as follows. In agreement with Roelvink et al. (2018), the short-wave breaking formulation of Daly et al. (2012) was always used. However, instead of using the option to compute the mean direction of the short-wave field with the stationary wave solver (i.e., the *single-dir* option), the numerical scheme for the wave propagation solver was reverted to the second-order upwind option. This choice was made because studies with a previous version of XBeach demonstrated good estimates of the IG wave energy (e.g., Bertin and Olabarrieta 2016; Lashley et al., 2019). The bottom friction was represented with a Manning formulation. The Manning coefficient was initially set to 0.019 $m^{-1}/_{3}.s$, which is representative of open sandy beaches (Smith et al., 1993). Still, the Manning coefficient was ultimately lowered to 0.015 $m^{-1}/_{3}.s$ to reduce the bias in the height of the IG waves, which remained underestimated after the dissipation of short-waves by breaking was calibrated. The short-wave dissipation coefficient (α) was first increased from 1.00 (default) to 1.15 to match the modelled (maximum) significant wave height at high tide with observations at the location closest to the shoreline (PT3). Then, XBeach's option to add a fraction (δ) of the instantaneous wave height (H) to the water column (h) when calculating maximum wave height (H_{max}), as described in Eq. (6), was tested and retained. This option was used with an adjusted value of the wave breaking criterion (γ). For instance, when using $\delta = 0.5$ and the recommended value of $\gamma = 0.52$ (Daly et al., 2012), Eq. (7) returns an adjusted value of 0.41 for γ. Therefore, a combination (δ, γ) of (0.5, 0.41) was used, which compared better with observations at all locations (see the following sections). As referred to in Section 3.1, the wave-current interactions had to be switched off in all simulations.

2.3.4. March 2020 and February 2019 bathymetries

As for the first study step, described in detail in Section 3, the first eight configurations were run over the full data coverage on 10 March 2020 to assess the representation of short- and IG waves in the surfzone; the last configuration (1D-NH) was used to simulate the high tide of 10 March 2020 along the profile P2. In a second step, described in detail in Section 4, the five 2DH configurations were used to simulate the overtopping and inundation scenarios. Simulations were repeated with 1D-NH along profiles P1 and P3. Details on the model's boundary conditions and scenarios used in each step are provided in the next section.

Different model bathymetries were used in each step. In both, the shore, the shoreface and the harbour access channel were surveyed in the scope of the national monitoring programme COSMO (COSMonline; https://cosmo.apambiente.pt/). In Section 3, the model validation was performed with the COSMO's digital elevation model (DEM) issued for August 2020 and completed with the beach survey from March 2020 (see Section 2.2.1). In Section 4, the inundation scenarios were run with COSMO's DEM from August 2019, completed with the beach and dune survey from February 2019 (see Section 2.2.1). Both bathymetries were first interpolated onto the 2D-LR grid, with the lower cross-shore resolution. Then, the bathymetries of the 1DH models and the refined 2D-MR and 2D-15 models were interpolated from the 2D-LR grid. By doing so, differences between models should only result from different resolutions and not from the inclusion of unresolved topo-bathymetric features in the lower resolution models.

2.3.5. Boundary conditions

Common conditions were imposed at the model's boundaries: absorbing-generating conditions were prescribed at the offshore boundary, and Neumann and wall conditions were prescribed at the lateral and lagoon boundaries, respectively. Primary offshore boundary conditions consist of two-dimensional (frequency and direction) spectra and water levels. These were imposed at the northwest and southwest corners of the local models after they were downscaled using the model workflow described in Appendix A. From the spectra, XB-SB combines spectral components to generate time series of wave height and water level and velocities (i.e., bound IG waves), which vary in time and space on the scales of wave-groups. Because the wave spectra do not have phase information, the phase of each spectral components is defined with a random function. By default, the random function is initialized with a random seed (i.e., option *random* = 1), so the same spectra used at a different time may produce a different wave time series. So, for the consistency of the calibration processes, boundary conditions were only generated once and reused while adjusting other parameters. Further details on the simulations period are given at the start of Sections 3 and 4.

2.3.6. Hydrodynamic output processing

Model outputs include the root mean square wave height (H), the sea surface elevation (η) and the depth average cross-shore velocity (u). These quantities were outputted as time series at 1 *Hz* at fixed point locations, as well as spatial fields, over the entire (1DH or 2DH) computational domain, of mean(), variance (σ^2), maximum and minimum values of each quantity over 17- to 30-min intervals. At fixed point locations, such as the PTs (Fig. 1), the modelled $H_{S,SW}$ was computed from the time varying H with Eq. (8), after Roelvink et al. (2009), while for the spatial outputs, it was computed as Eq. (9), where σ_H is the standard deviation of H.

$$H_{S,SW} = \sqrt{2 \times \overline{H^2}} \quad \text{Eq. 8}$$

$$H_{S,SW} = \sqrt{2 \times \left(\overline{H} + \sigma_H^2\right)^2} \quad \text{Eq. 9}$$

In Eqs. 8 and 9, H is computed by XB-SB's short-wave average propagation solver which does not account for the wave reflection at the shoreline. As a results, the modelled values of $H_{S,SW}$ miss the reflected energy that may be present in the observations (and also in XB-NH) and particularly near the shoreline (Baquerizo et al., 1997).

For the fixed point outputs in both the XB-SB and XB-NH models, the IG significant wave height ($H_{S,IG}$) and mean period ($T_{m02,IG}$) were computed for the η time series with Eqs. (1)–(3) and $(f_{min}, f_{max}) = (0.001, 0.04)$ *Hz*, like for the hydrodynamic data. For XB-NH, $H_{S,SW}$ was also computed with Eqs. (1)–(3) and the frequency boundaries set equal to those for the PT record. Then, for both fixed point and spatial outputs, the total significant wave height ($H_{S,Tot}$) in XB-SB and XB-NH were compared $H_{S,Tot}$ was computed with Eqs. (10) and (11) for XB-SB outputs, whereas in XB-NH $H_{S,Tot}$ is directly equal to $H_{S,\eta}$, given by Eq. (11) and where σ_η is the standard deviation of the modelled sea surface elevation.

$$H_{S,Tot} = \sqrt{H_{S,SW}^2 + H_{S,\eta}^2} \quad \text{Eq. 10}$$

$$H_{S,\eta} = 4 \times \sigma_\eta \quad \text{Eq. 11}$$

When overtopping occurred, instant discharges were computed at fixed point stations located at the dune crest. In both XB-SB and XB-NH, the instantaneous Eulerian cross-shore velocity (u) and sea surface elevation (η) were outputted from the shallow water equations solver, and the overtopped volumes were integrated over time from the instantaneous discharges computed as $q_u(t) = u(t) \times (\eta(t) - z_b)$, where z_b is the model's local bottom elevation. During a given simulation, the resulting inundation extents were defined from areas of the computational domain where, at some point in time, η exceeded z_b.

2.3.7. Computing overtopping exposure

To estimate the spatial variations of the exposure to flooding under a given forcing or for a given model configuration, a set of ten repeated simulations was performed with the same forcing inputs and with the option *random* = 1. From each set of simulations, a spatial exposure index was defined ranging from zero to one: for instance, areas inundated in one, five or ten simulations were mapped with an exposure index of 0.1, 0.5 and 1.0, respectively. In all simulations, the model

bathymetry remained unchanged during the simulations as the morphological evolution was deactivated for the mapping. Each simulation lasted for 22 min, only including a 5 min spin-up because the elevation at the boundary remained constant (i.e., no tidal signal). Hence, the inundated areas were mapped as areas where the sea surface elevation exceeded the bottom elevation at some point during the remaining 17 min. Exposure maps were produced for the 2DH model configurations described in Table 1, with the forcing scenarios described in **section 4.1**. For those scenarios, the overtopping discharges were also computed with the configuration 1D-NH, run along profiles P1 and P3 in Fig. 3, and compared to those computed in 2DH.

3. Nearshore waves calibration and validation

3.1. 2DH and 1DH scenarios

The first set of simulations aimed to calibrate and validate the short and IG waves in the local 2DH model. The simulations were performed in a Linux environment with 58 CPUs, on an AMD EPYC 7 501 server (2.0 GHz). In the case of the 2D-LR domain (Table 1), with about 1 400 grid nodes per CPU, the computational time was below 11% of real time, while in the 2D-MR case (~27 600 grid nodes per CPU) it reached 34% of the 13-h simulated period. These 13 h overlap with the hydrodynamic data collected in March 2020 (**Section 2.2**). In this case, the variability generated at the boundary by XB-SB on the wave-group scale adds to the variations and trends computed with the regional and cross-scale models: spectra for computing the boundary conditions were updated every 30-min. An example of the directional wave spectra is given on the left panel of Fig. 4, which corresponds to the high tide of March 10; the spectra on the centre and right panels correspond to the forcing used in **Section 4**. These three spectra were downscaled as described in Appendix A, and consist in two-dimensional arrays of 36 frequency (f) and 36 directions (θ).

To minimize the error propagation, the elevation imposed at the local model boundaries was unbiased based on the differences between the cross-scale model and the tidal gauge (Appendix A,Table A.2). The runs started at the mid-ebb tide, at 6h00 UTC, and proceeded over a complete tidal cycle (Fig. 5). At the harbour's tidal gauge, the root-mean-square differences between modelled and observed elevations equalled 5.2 cm. The modelled horizontal velocities were on the same order of magnitude at a shared location with the cross-scale model, within the harbour's access channel (Fig. 5). Therefore, beyond interacting with the non-uniform morphology, IG waves will also interact with the tidal jet created by the schematized estuary. In terms of short-waves, however, the wave-current interaction in the model had to be switched off, meaning the short-wave propagation and transformation were solely impacted by the morphology (i.e., shoaling, refraction and breaking). Attempts to consider these wave-current interactions within XBeach systematically led to instability. The models' quantitative performances were evaluated for all the 2DH configurations in Table 1, as well as for the 1DH ones along profile P2 (Fig. 3) excepting 1D-NH.

The 1D-NH configuration was used in a second set of simulations, focusing on the high tide of 10 March 2020, at 15h25 UTC (± 15 min). These simulations aimed at a qualitative comparison of 1D-NH with 2D-WR, 2D-LR as well as with the PT record. For consistency with the PTs, the actual tidal signal was accounted for as the mean water level first rose by 11 cm over a half-hour spin-up. Then the tidal level stabilised around 1.76 cm ALTH39 during the last 30 min of simulations, over which the results were processed. The models were run for an hour and with a single wave spectrum (and the random phase deactivated, i.e., *random* = 0), with mean wave parameters of 2.17 m, 12.9 s and 292°N, for, respectively $H_{S,SW}$, T_P and the mean direction.

3.2. Nearshore short- and IG wave results

For the default (2D-WR) and calibrated (2D-LR) configurations, Fig. 6 presents the results of the model at the locations PT1-3 indicated in Fig. 1e. Despite a zero bias at the tidal gauge, all model configurations of XB-SB overestimated the mean elevation observed at nearshore PTs (bias of +9 cm, +17 cm and +2 cm, respectively from PT1 to PT3, in the case of 2D-LR). Still, with the default short-wave breaking parameters (2D-WR and 2D-UP), the high tide peak of the modelled $H_{S,SW}$ was underestimated compared to the observed $H_{m0,SW}$ (see Table B2 for details). Although the short-wave reflection at the shoreline is not accounted for in XB-SB, this underestimation decreased towards the shore. Overall, the match with the PTs was improved by setting δ equal to 0.5 (2D-LR, Fig. 6), while the coefficient α in **Eq. (5)** was also increased to 1.15 to better fit with the dissipation profile from PT1 to PT3. The resulting root-mean-square differences were on the order of 11 cm–14 cm for 2D-LR, corresponding to differences on the order of 11%–15% when normalized by the average measured $H_{m0,SW}$. However, the overestimation of $H_{S,SW}$ in the lower stage of the tide could not be resolved and led to the overall overestimation, as depicted by the remaining positive biases (Table B1). Beyond improving the shape of the $H_{S,SW}$ curves, the calibration of the short-wave dissipation substantially improved the match between of the observed $H_{m0,IG}$ and the modelled $H_{S,IG}$. Despite the height of modelled IG waves remained slightly underestimated in 2D-LR, differences with the observation were reduced by a factor of 1.7–3.6 compared to those in 2D-WR (Fig. 6); most of this improvement should be attributed to the less diffusive second order

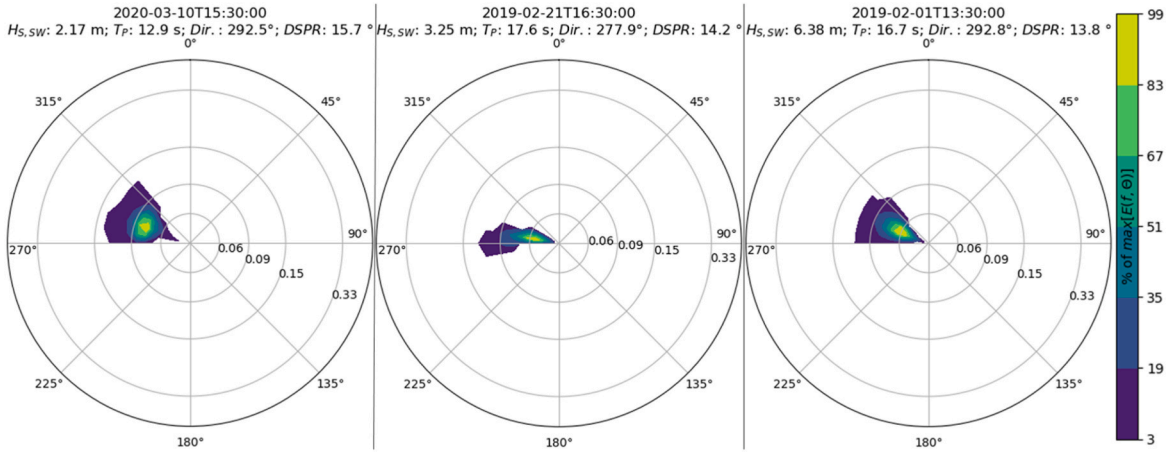

Fig. 4. – Two-dimensional, wave energy spectra $E(f,\theta)$, given in % of max $(E(f,\theta))$, used to force the model boundary in Fig. 8 (left spectrum), Figs. 9 and 11 (middle) and Figs. 10 and 11 (right).

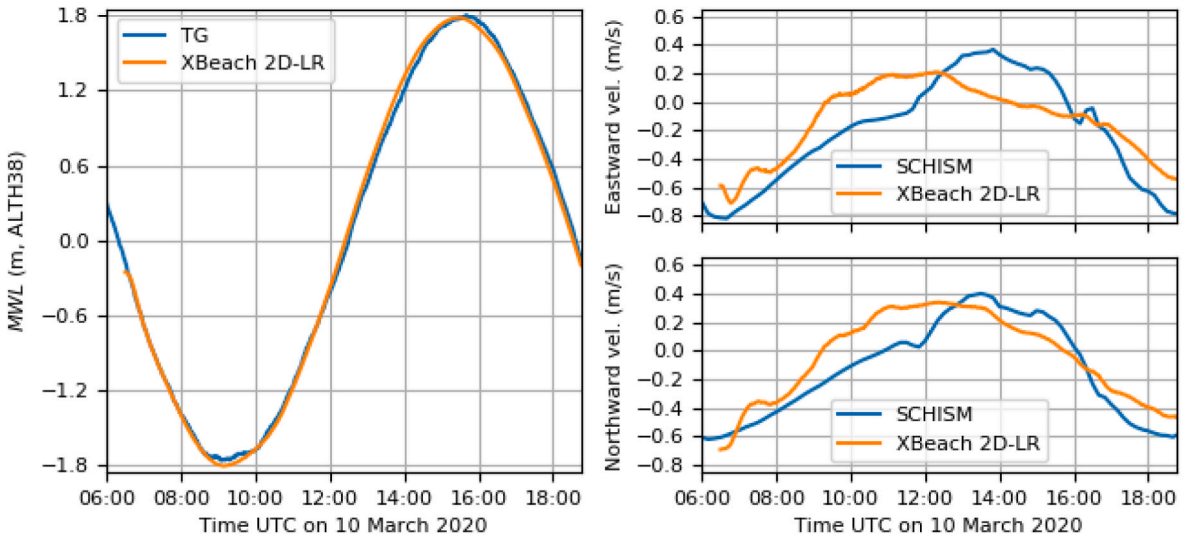

Fig. 5. – Left: observed (TG) and modelled (XBeach, 2D-LR) mean water level (MWL) at the IH's tidal gauge; right: modelled horizontal velocities in the cross-scale (SCHISM, see **Appendice A** for details) and 2D-LR model within the harbour's access channel.

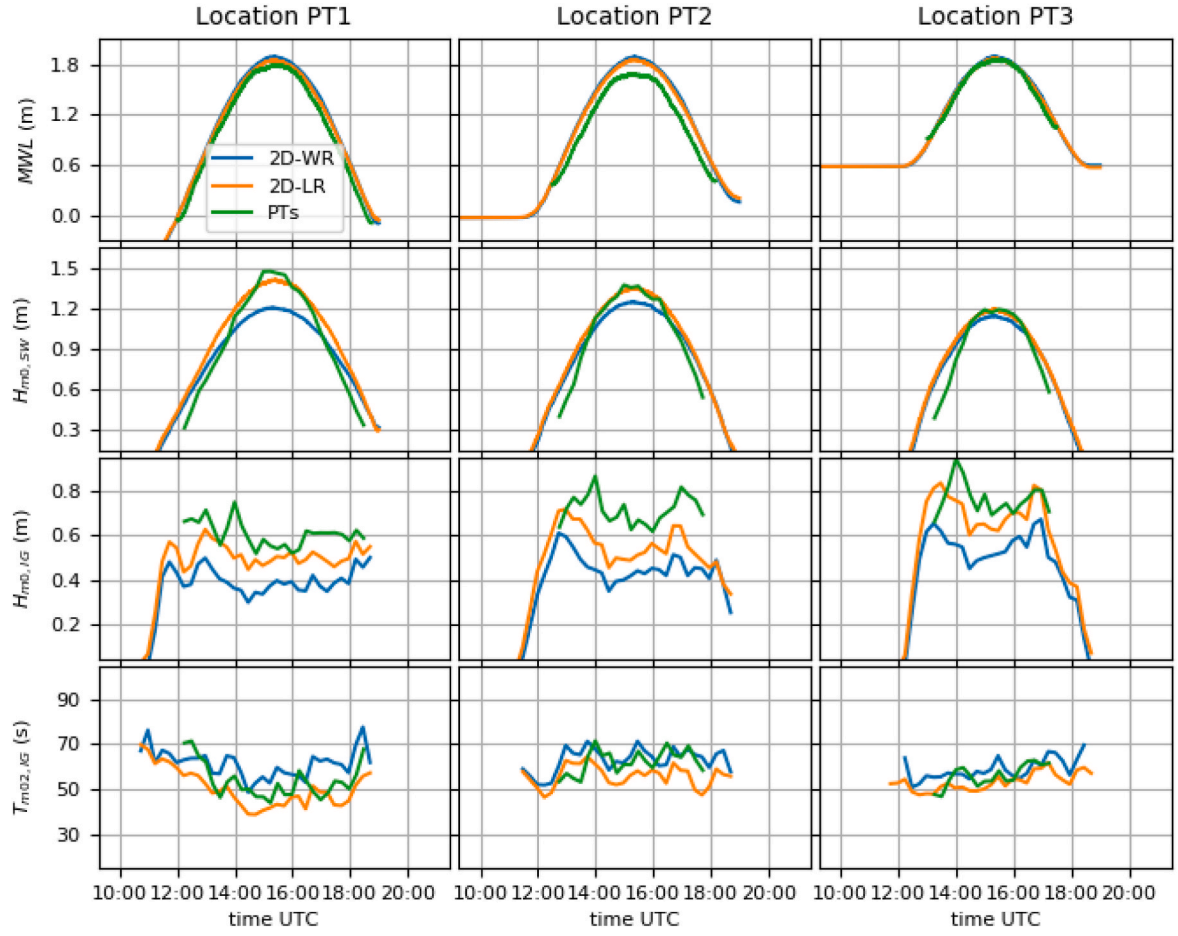

Fig. 6. – Observed and modelled nearshore mean water levels (MWL) and mean wave parameters at the PTs' locations shown in Fig. 1e; the modelled curves were obtained for simulations 2D-WR and 2D-LR (Table 1).

upwind scheme (2D-UP, see Table B.3 for details). The improvements of the IG wave height had little effects on the mean period $T_{m02,IG}$ (see Table B.4 for details), while both the variations, of the IG wave height and mean period, followed the trends observed throughout the tidal cycle (Fig. 6).

Contrary to the 2DH models, the 1DH models mostly overpredicted the height of the IG waves, although, as depicted in Fig. 7 for 1D-MR, the overprediction diminished shoreward and/or with higher grid resolution. The same occurred with the IG mean wave period, which was overpredicted from a few seconds up to about 8 s on average (for details,

see Tables B3 and **B.4**). However, the model predictions deteriorated when increasing the model's resolution, and, within the 1DH models, the 1D-MR appeared to represent better the cross-shore transformation of the waves at Cova-Gala beach. Therefore, 2DH runs were performed with the cross-shore grid-spacing divided by two compared to the original model (2D-MR and 2D-15). Increasing only the cross-shore resolution (2D-MR) did not lead to significant improvements. In particular, the negative bias remained in $H_{S,IG}$. So, to minimize this negative bias, the Manning coefficient was lowered to 0.015 $m^{-1/3}.s.$ Although this value lies at the lower end of the typical range of Manning coefficients for sandy environments, it is larger than, for instance, the equivalent Chezy coefficient used by Bertin et al. (2020). Here, the smaller friction coefficient first resulted in model instability with the original model resolution (similar to 2D-LR). However, this was not the case with the higher cross-shore resolution (2D-15), leading to improved comparisons with the mean wave parameters measured at all PT locations (Fig. 7; for details on 2D-MR and 2D-15, see Tables B3 and B4).

3.3. Spectral energy distribution

After the above quantitative performance of the model, a qualitative description follows, aiming at picturing how the calibrated 2DH model (2D-LR in this case) represents the sea surface oscillations in the nearshore compared to the default configuration (2D-WR) and the non-hydrostatic configuration (1D-NH). The shape of the frequency spectrum was very similar in 2D-MR and 2D-15 compared to 2D-LR. So the comparison focuses on the differences with 2D-WR and 1D-NH, along the profile P2 (Fig. 3).

Fig. 8a presents the evolution of $H_{S,Tot}$, $H_{S,SW}$ and $H_{S,IG}$ in the last hundred metres of the short-wave shoaling zone to the shoreline in 2D-LR and 1D-NH; the solid lines ($H_{S,Tot}$) were extracted from the XBeach spatial outputs and computed as **Eqs. 10** and **11**, while $H_{S,SW}$ and $H_{S,IG}$ were computed from fixed output points and are represented as symbols like the observations from the PTs. In the shoaling zone, the values of $H_{S,Tot}$ were overall in good agreement in the two models. Although $H_{S,SW}$ in 1D-NH was slightly smaller than in 2D-LR, it was somehow compensated by the slightly larger $H_{S,IG}$. Differences between the two models increased in the surfzone, i.e., shoreward of the $H_{S,Tot}$ maxima, and over the steeper foreshore, where the total energy was higher in 1D-NH. Still, the 2D-LR better fitted the differentiated short and IG wave energies measured at the PT's locations. Differences in the wave height were accompanied by small discrepancies between modelled set-down and set-up, which were overall spatially in good agreement in both models, although they were more pronounced in 1D-NH (Fig. 8b). Finally, the spectral analysis also confirmed the good agreement between 2D-LR and the observations, in particular, at location PT1, where the double-peaked shape of the frequency spectrum was well reproduced and improved with the model calibration (Fig. 8c). However, the energy in the lower frequencies of the IG band (i.e., periods greater than 40 s) remained underestimated in the 2D-LR and was overestimated in 1D-NH (Fig. 8d).

4. Overtopping and inundation extents

4.1. Scenarios

The calibration of the hydrodynamic model was intended to find the

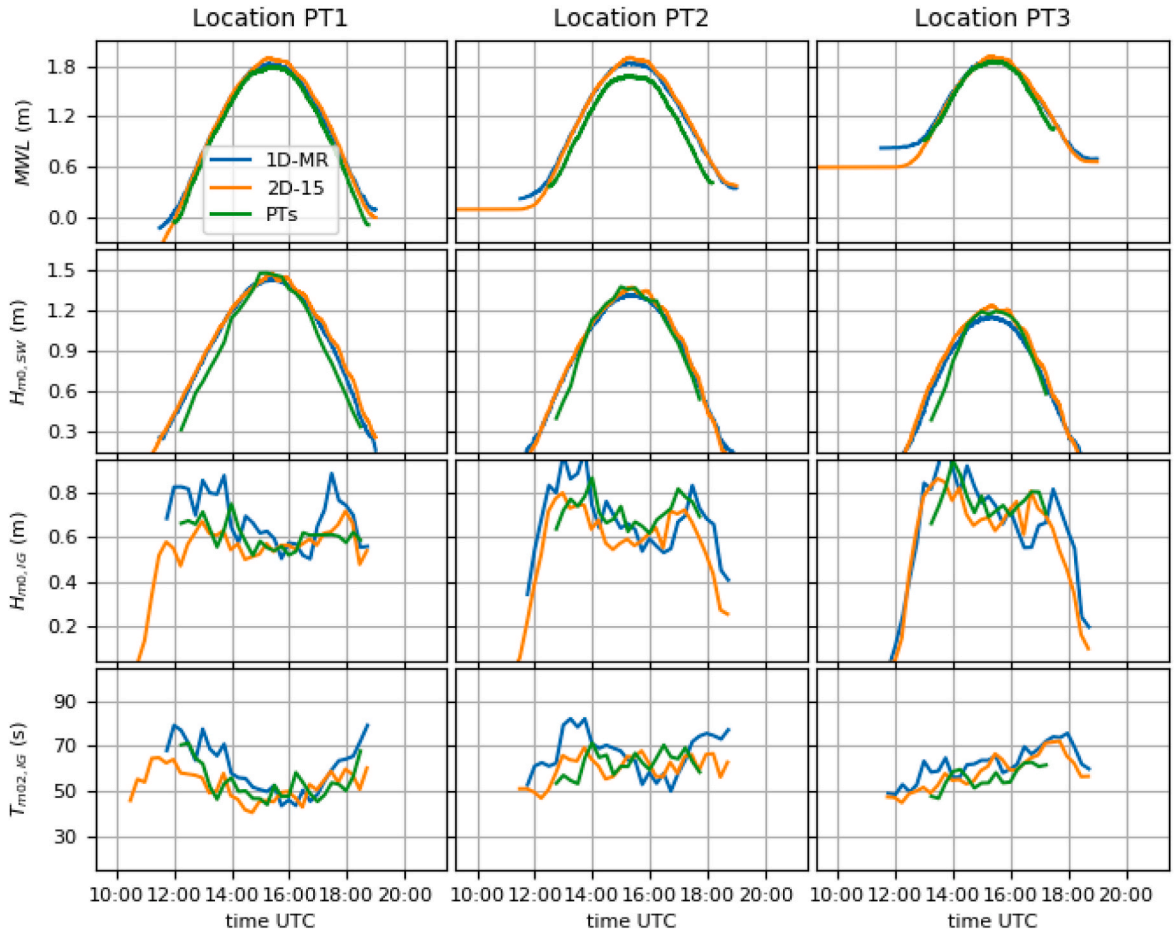

Fig. 7. – Observed and modelled nearshore mean water levels (MWL) and mean wave parameters at the PTs' locations shown in Fig. 1e; the modelled curves were obtained for simulations 1D-MR and 2D-15 (Table 1).

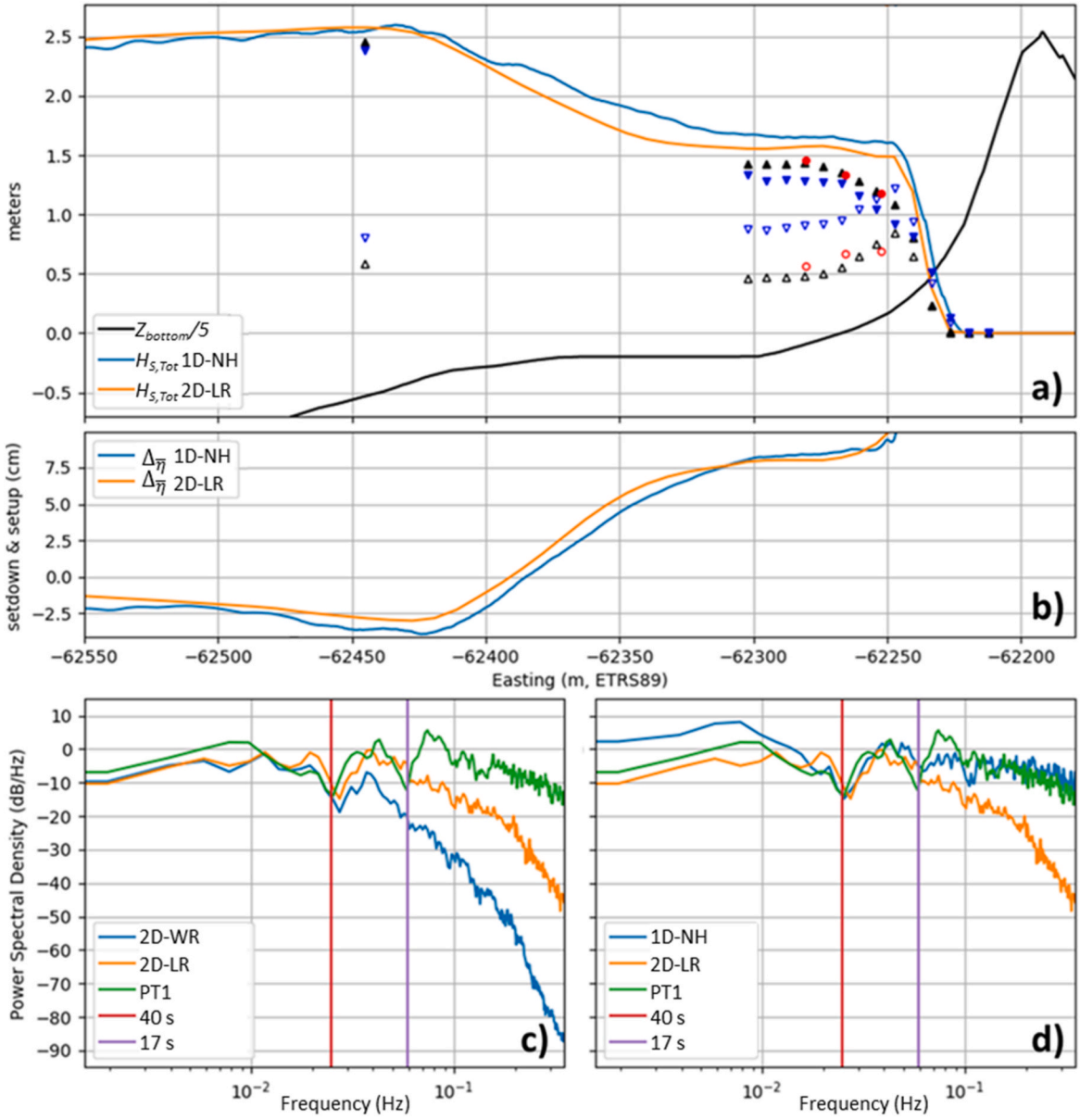

Fig. 8. – a) Modelled $H_{S,Tot}$ at high tide with 2D-LR and with 1D-NH; filled symbols ▲,▼ and ● stand for $H_{S,SW}$, respectively for fixed point outputs from 2D-LR and 1D-NH, and at the PT locations; empty symbols are the same but for $H_{S,IG}$; **b)** modelled set-up and set-down anomalies ($\Delta_{\overline{\eta}}$) in both 2D-LR and 1D-NH models; **c)** frequency spectra of the modelled surface elevation with 2D-WR and 2D-LR surfbeat models, as well as for the observation at sensor PT1; **d)** same as **c)** but with elevation from the 1D-NH instead in place of 2D-WR.

best parametrization to represent nearshore waves in XBeach. The calibrated parametrization is tested for two overtopping situations occurring under contrasting scenarios of combined water level and sea state. The first scenario was defined after observations of a small overtopping event at the southern limit of Cova-Gala under moderate wave forcing (Fig. 1d); the second aimed to test the model's robustness under energetic forcing. For each combination of model configuration and forcing scenario, sets of ten 22-min simulations were performed.

These were used to create exposure index maps and the overtopping discharges presented respectively in **Section 4.2** and **4.3**, following the methods described in **Sections 2.3.7** and **2.3.6**, respectively.

The observed event took place on 21 February 2019 at high tide. At the XBeach model's offshore boundary, the cross-scale model predicted a mean water level (MWL) of 1.77 m ALTH38. Predicted waves had a significant height of 3.25 m, a peak period of 17.6 s, and a near shore-normal incidence of 277°N. The modelled directional spreading (DSPR) was on the order of 14° (i.e., parameter $s = 32$). Along with the impact of the parameters issued from the model calibration, the impact of the spectral characteristics of the wave spectrum on the modelled inundation were tested. After the downscaled wave spectra were used to force the five defined 2DH configurations (Table 1), the 2D-LR configuration was also forced with two JONSWAP spectra. The first JONSWAP spectra was defined with the mean wave parameters and with the modelled value of the DSPR, the second with XBeach default value of $s = 10$ (i.e., DSPR of 24.4°).

The second scenario addresses the question of the robustness of the model under energetic forcing, accompanied by expected high overtopping rates. The energetic waves were taken from the hindcast of the storm Helena in early February 2019 (Fig. 4, right panel, and Figure A3). At the peak of the storm, modelled offshore mean wave parameters ($H_{S,SW}$, T_P, Dir. and DSPR, respectively of 8.90 m, 16.9 s, 300°N and 13°) match the values reported in Section 2.1 from Oliveira et al. (2018). At the south-western 2DH XBeach model's corner, the integrated spectrum had a significant height of 6.38 m, a peak period of 16.8 s, and an

oblique incidence of 293°N (similar to the incidence during the field campaign of March 2020). The directional spreading was just below 14° ($s = 34$). These waves were associated with a combined tide plus atmospheric storm surge water level specified as 2.20 m above the MSL (currently at +0.19 m ALTH38, see Appendix A for further details). Having a return period of ~70 years (Fortunato et al., 2019), this water level was considered severe enough for the present objectives.

Results for the two scenarios were analysed in distinct areas. For the first scenario, model results were analysed where inundation was observed, i.e., at the southern end of the model domain and away from the inlet jetties and delta (Figs. 1d and 3). For the second scenario, model results were analysed in the shelter of the harbour's southern jetty (Fig. 3). Despite the shelter from the shallow ebb-delta, and the steep foredune profile armoured with riprap, this latter area is known to be subject to overtopping, although less frequently than the lower sandy dune for which the observations were available.

The same bathymetric DEM was used in both scenarios, in which the elevation across the beach and foredune was interpolated from a photogrammetric survey dating from 11 February 2019 (**Section 2.3.2**). Again, when the model discretization was refined (i.e., in 1D-NH, 2D-MR and 2D-15 simulations), the bathymetry was merely interpolated from the 2D-LR.

4.2. Mapping of overtopping exposure

Fig. 9 presents the exposure maps produced for the five 2DH configurations (Table 1), combined with the moderate forcing scenario of 21 February 2019 ($H_{S,SW}$ and MWL respectively of 3.25 m and 1.77 m ALTH38). The random boundary conditions were saved and kept identical for all maps. This way, the differences between maps arise either from the numerical scheme for short-wave propagation, the short-wave breaking parameterization (γ, δ), the cross-shore grid resolution or/and from the bottom friction coefficient. In the observation data, two small and larger overtopping deposits were present. The low resolution, calibrated configuration (2D-LR) predicted overtopping at some point in the larger patch but missed the two-small ones. The modelled extent of the larger patch matches quite well the observed one, although the exposure index remained relatively low: the area got inundated in less than 50% of the simulations. The exposure decreased when switching to the default *warmbeam* scheme (2D-WR[1]), and was null when using the default $\delta = 0.0$ (2D-UP). Similar to 2D-UP, no overtopping occurred when forcing the 2D-LR with a generic JONSWAP wave spectrum (with either the default or hincasted DSPR). When the cross-shore resolution was increased (2D-MR), the inundation in the larger patch area became systematic: the exposure index equals one in most of the observed patch. One of the two small patches also became inundated when the models' resolution in the foredune slope increased, with the second small patch only getting inundated in the model when the Manning's coefficient was lowered (2D-15).

Exposure maps were also reproduced for the energetic forcing scenario ($H_{S,SW}$ and MWL respectively of 6.38 m and 2.39 m ALTH38), for the configurations 2D-LR, 2D-MR and 2D-15. Fig. 10 presents the results focusing on the inundation-prone area just south of the harbour entrance (Fig. 3, northern box). This time, refining the model resolution did not just increase the exposure index behind the dune crest but also widened the exposed area. Indeed, compared to 2D-LR, the exposed area in 2D-MR extended across the entire barrier width and the water reached the back-barrier estuary. Then, reducing the bottom friction coefficient (2D-15) further increased the frequency and the extent of inundation. In all three sets of ten simulations, the model remained numerically stable and was shown to be able to handle overtopping rates large enough to reach the back-barrier estuary. In the next section, those overtopping

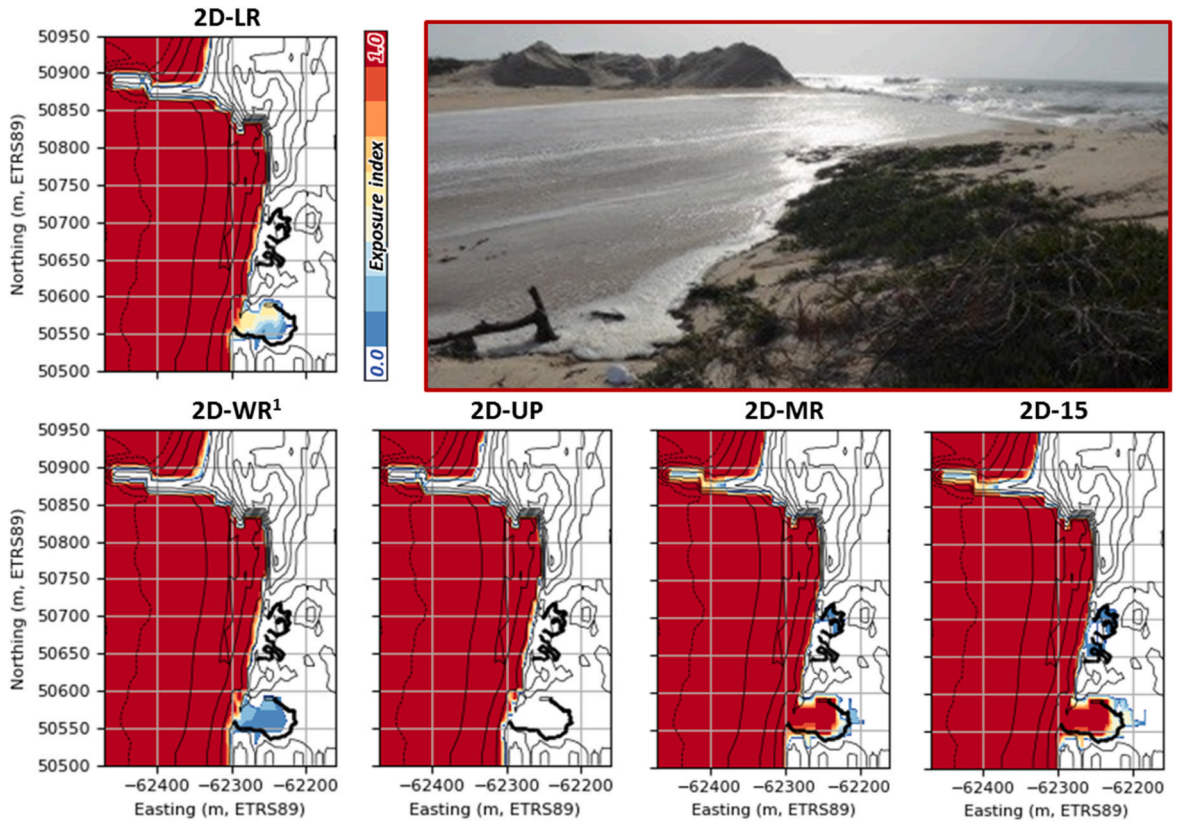

Fig. 9. - Picture: photograph of the sandy dune being overtopped by a wave at high tide on 21 February 2019; maps of exposure index: created with configurations 2D-LR, 2D-WR[1], 2D-UP, 2D-MR and 2D-15 listed in Table 1, forced with the downscaled directional wave spectra shown in Fig. 4, centre panel; the thin black contours on the maps are the model's DEM isocontours at a 1 m step, and the thick black lines are the surveyed wrecklines from the observed overtopping (see Fig. 3 for mapping extent location: southern box).

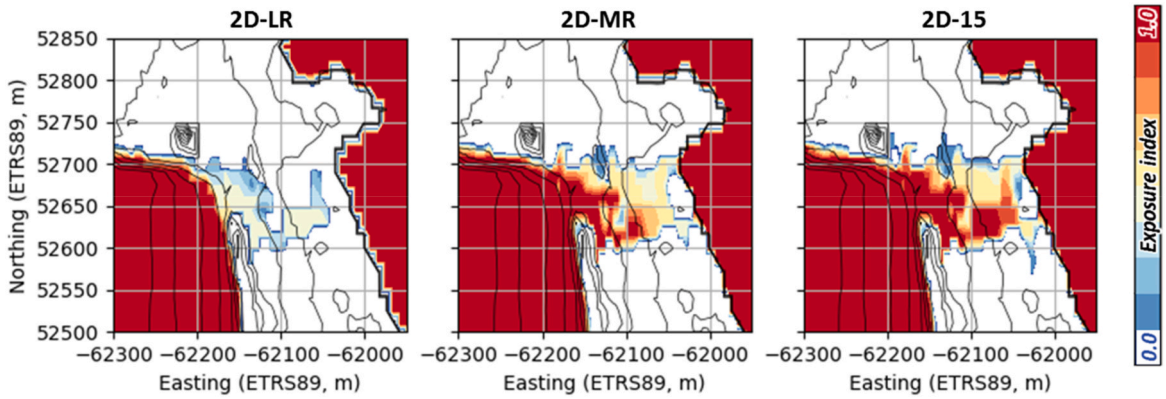

Fig. 10. – Maps of the exposure index for the directional wave spectra from the storm Helena in early February 2019 (Fig. 4, right panel), combined with a ~70-year return period water level (see Fig. 3 for mapping extent location: northern box).

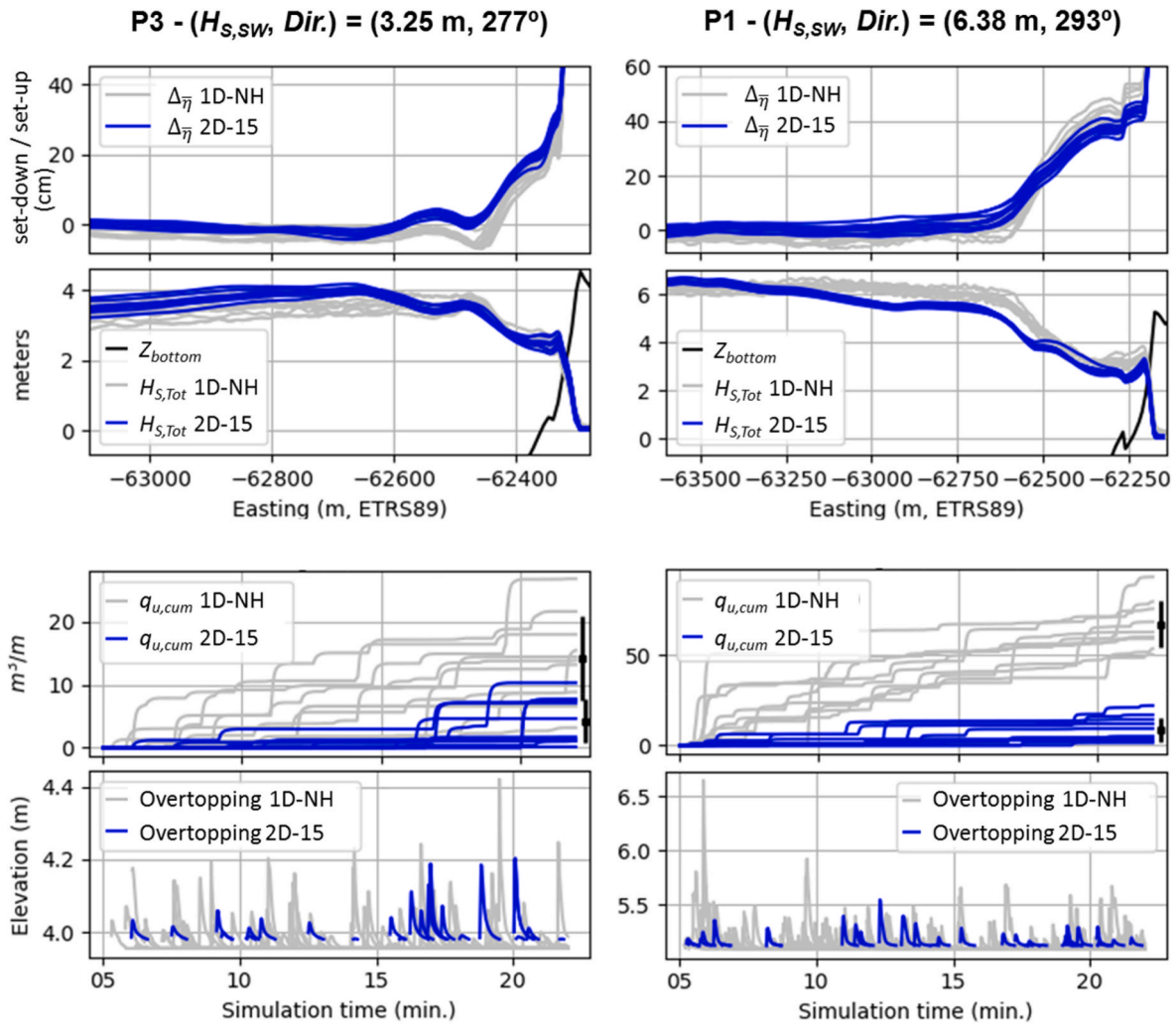

Fig. 11. – From top to bottom, set-up and set-down anomalies ($\Delta_{\overline{\eta}}$), total significant wave height ($H_{S,Tot}$; Eqs. 10 and 11), cumulative volumes of overtopped seawater ($q_{u.cum}(t) = \int q_u(t)dt$) and overtopping events ($\eta(t) > z_b$) for the sets of ten XB-SB (2D-15, in blue) and ten XB-NH (1D-NH, in grey) simulations, the vertical black bars after the curves of cumulative volumes show the mean±the standard deviation for the four sets of simulations after 17 min.

rates were compared to those obtained with the non-hydrostatic solver of XBeach.

4.3. Overtopping volumes

The presented exposure maps implicitly resulted from the model's capacity to simulate the volume of water overtopping the dune's crest and the shore-parallel defence structures. To describe this process and

how the 2DH surfbeat model behaves with respect to its 1DH phase-resolving counterpart, overtopping volumes were computed for the sets of simulations with 2D-15 and compared with similar sets of simulations performed with 1D-NH for profiles P1 and P3 (Fig. 3).

The moderate forcing scenario was run for profile P3. The left panels in Fig. 11 show the results in terms of wave-induced set-down and set-up, total significant wave height, and cumulative overtopped volumes, the last panel identifying the frequency of overtopping events. In both models, the set-down presented a double-peaked shape. In 2D-15, the minimum set-down occurred further offshore and was less pronounced than in 1D-NH. Also, both $H_{S,Tot}$ and the set-up were larger in the 2D-15 simulations, even though the energy started to dissipate further offshore. However, under these near shore-normal short-waves and away from the ebb-tidal delta influence, the average overtopping volume in the surfbeat simulation was about a third of the one calculated in the NH simulations. The overtopping was also much less frequent in the 2DH-surfbeat simulations.

In similar fashion, the energetic forcing scenario was run for profile P1 (Fig. 11). Like in the simulation presented in **Section 3.3**, the short-waves approached the coast with an angle of incidence about 15° higher than in the previous case. Again, $H_{S,Tot}$ peaked closer to the shore and dissipated over a shorter distance in the 1D-NH simulations. But in this case, $H_{S,Tot}$ was substantially higher in the surfzone and at the shoreline in 1D-NH compared to 2D-15. The resulting set-up and set-down were more pronounced in 1D-NH, although the anomalies were in phase in both approaches. In these conditions, the differences in overtopping rates and frequency were even greater between 1D-NH and 2D-15: on average, in 1D-NH the overtopping volume after 17 min was 7.5 times greater than in 2D-15.

5. Discussion

The above results were produced to discuss how far the surfbeat solver of XBeach can be pushed for mapping wave-induced flooding, considering that this capacity is relevant for applications in areas extending several kilometres alongshore with irregular geometries. The starting point was to build a relatively coarse and numerically efficient model: the initial model was large enough to account for features like the harbour entrance and the large ebb-tidal delta, but its resolution was just fine enough to represent submerged shoals and structures like groins or inlet jetties. Considering IG waves with a mean period just above 50 s, the dimensionless wavelength of the model's grid was above 50 only up to approximately the seaward edge of the ebb-tidal delta (i.e., the 11 m depth contour) and dropped below 20 across the intertidal beach (i.e., shoreward of the 1.5 m depth contour).

5.1. Calibrating nearshore waves

5.1.1. Short-wave breaking

Regarding nearshore hydrodynamics, the resolution of the coarsest grid (from 15.0 m to 6.5 m) did not appear as a major limiting factor. Indeed, the quality of the initial model implementation was greatly improved after it was calibrated with a limited amount of in-situ data. The data first helped to scale the short-wave energy dissipation due to breaking. Initially, the dissipation profile was not steep enough. This could have been solved by increasing the wave breaking criterion (γ) to delay the short-wave breaking, combined with a higher wave dissipation coefficient (α). However, to limit the increase of α to 1.15, γ was scaled by setting the coefficient δ, in **Eqs. 6 and 7**, equal to 0.5. Fig. 12 shows the impacts of this parameterization (2D-LR and 2D-15) for the same forcing conditions as in Fig. 7. Prior to short-wave breaking, the total significant wave height ($H_{S,Tot}$) in XB-SB peaks at slightly lower value than with the default breaking coefficients (2D-UP). As a result, the set-up and set-down profile are less pronounced with the calibrated coefficient, the curve with the non-hydrostatic (1D-NH) model lying in between the two XB-SB parameterizations (Fig. 7b). Then within the inner surfzone, the dissipation profile of the significant short-wave height ($H_{S,SW}$) and of $H_{S,Tot}$ almost perfectly match the one measure with the PTs. Also, because the short-wave height is time-dependent in XB-SB, the larger waves start breaking in relatively shallower waters as soon as δ is greater than zero. Hence, in addition to the improvement of the short-wave dissipation profile, slightly more energy is being transferred to the IG band.

5.1.2. Choice of the numerical scheme

While the calibration of the short-wave breaking did improve the modelled level of IG energy, the greatest improvement of the spectral shape was achieved by reverting the default numerical scheme to the second-order upwind scheme without additional numerical diffusion. Referring to Roelvink et al. (2018), and supported by smaller modelled IG mean wave periods, switching the numerical scheme may have steepened the wave groups compared to the *warmbeam* scheme. However, the overall best agreement with the data, even after refining the model grid, suggests the second-order upwind scheme was well-suited for the model's dimension and grid spacing. Then, according to the shape of the frequency spectrum, the underestimation of the IG mean

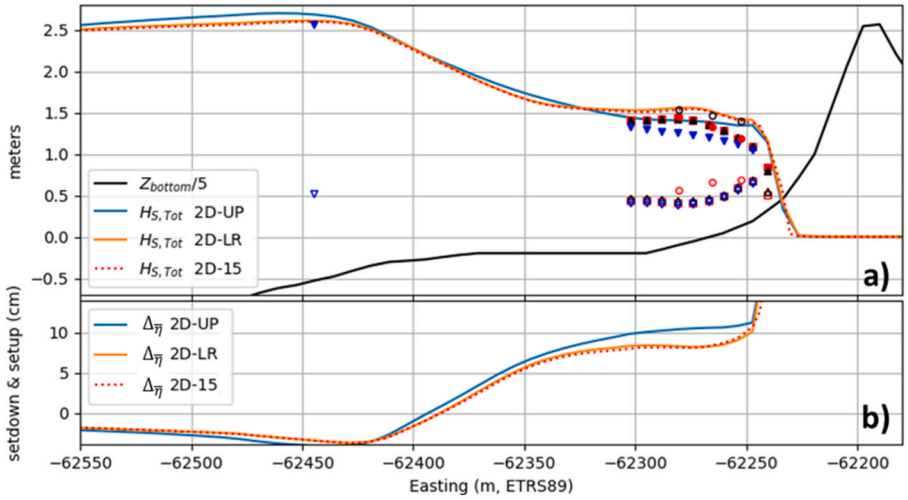

Fig. 12. – a) Modelled $H_{S,Tot}$ at high tide with XB-SB and for the high tide of 10 March 2020 (left panel spectrum on Fig. 4), filled symbols ▲,▼, ■ and ● stand for $H_{S,SW}$, respectively for fixed point outputs from 2D-LR, 2D-UP and 2D-15 models, and from the PT1-3, empty symbols are the same but for $H_{S,IG}$; **b)** associated modelled set-up and set-down anomalies ($\Delta_{\overline{\eta}}$) in both 2D-LR, 2D-UP and 2D-15 models.

period seems to be due to an underestimation of IG energy at frequencies below 0.025 Hz (i.e., periods greater than 40 s) rather than to a spurious numerical behaviour. Indeed, although the calibration improved the model estimations of the mean wave parameters, the energy in the (lower) IG bands remained underestimated.

5.1.3. Wave forcing and remaining uncertainties

The remaining underestimation of the IG wave height was not mitigated by refining grid. This suggests that the remaining bias was not due to an insufficient dimensionless wavelength. However, the simulations in **Sections 3** and **4** corresponded to narrow-banded sea states (i.e., DSPR below 15°), and it was expected that using a directional wave spectrum downscaled from WW3 and WWM (within SCHISM) was important for the prediction of nearshore IG waves. Indeed, when using mean wave parameters as inputs in **Section 4**, no overtopping was modelled when specifying only of the downscaled directional spreading. In this case, XBeach's default value for the JONSWAP peak enhancement factor was conserved (i.e., 3.3). However, Mazzaretto et al. (2022) stressed that, on the western margin of the world's continent, during the greatest storm this parameter could exceed twice this default value. This means the spectrum would be narrower, leading to greater modelled energy in the IG band (Van Dongeren et al., 2003). Likewise, Nicolae Lerma et al. (2017) also stressed the importance of accurate wave spectra for representing nearshore IG spectra and runup with phase-resolving models. Still, it is very likely that uncertainties remain on the quality of directional wave spectra modelled with wind-wave generation models (e.g., Alday et al., 2022), and/or on the validity range of the narrow-banded spectrum approach (Van Dongeren et al., 2003) for transforming it into wave-group boundary conditions in XBeach. Considering these uncertainties, adjusting the bottom friction appeared as an acceptable solution to tune the IG wave energy in the model. An alternative remediation would be the *single-dir* option (Roelvink et al., 2018) referred to in Section 2.3.1. However, this option remained unexplored due to unexplained convergence issues with the stationary wave solver in the XBeach version used here in.

5.2. Impacts on modelled overtopping exposure

5.2.1. Impact of short-wave settings

Following the calibration of the model settings in **Section 3**, the second round of simulations in **Section 4** used surveyed inundation extents to define a method for mapping the exposure to overtopping directly from XBeach. Based on the defined method, the survey data and exposure maps were used to further validate the model parameterization. In these additional simulations, all the settings related with the short-wave representation have impacted the modelled exposure (Fig. 9). Indeed, either considered or removed individually, the second-order upwind scheme, the short-wave breaking parameterization, and the directional wave spectrum, respectively, either improved or deteriorated the agreement between the maps and the observations. Following on Fig. 9, drawn for a moderate forcing, Fig. 13 exemplifies how the short-wave solver's settings alter the modelled sea surface elevation under energetic conditions. First, the less diffusive second-order upwind scheme (2D-UP) generates higher sea surface oscillations ($H_{S,\eta}$; +8.3% at peak near Easting = 62 200 m) and higher maximum sea surface elevation (η_{max}), up to the shoreline (Fig. 13a). This occurs while the short-wave height ($H_{S,SW}$) dissipates slightly faster in the surfzone while remaining similar to the simulation with the *warmbeam* scheme (2D-

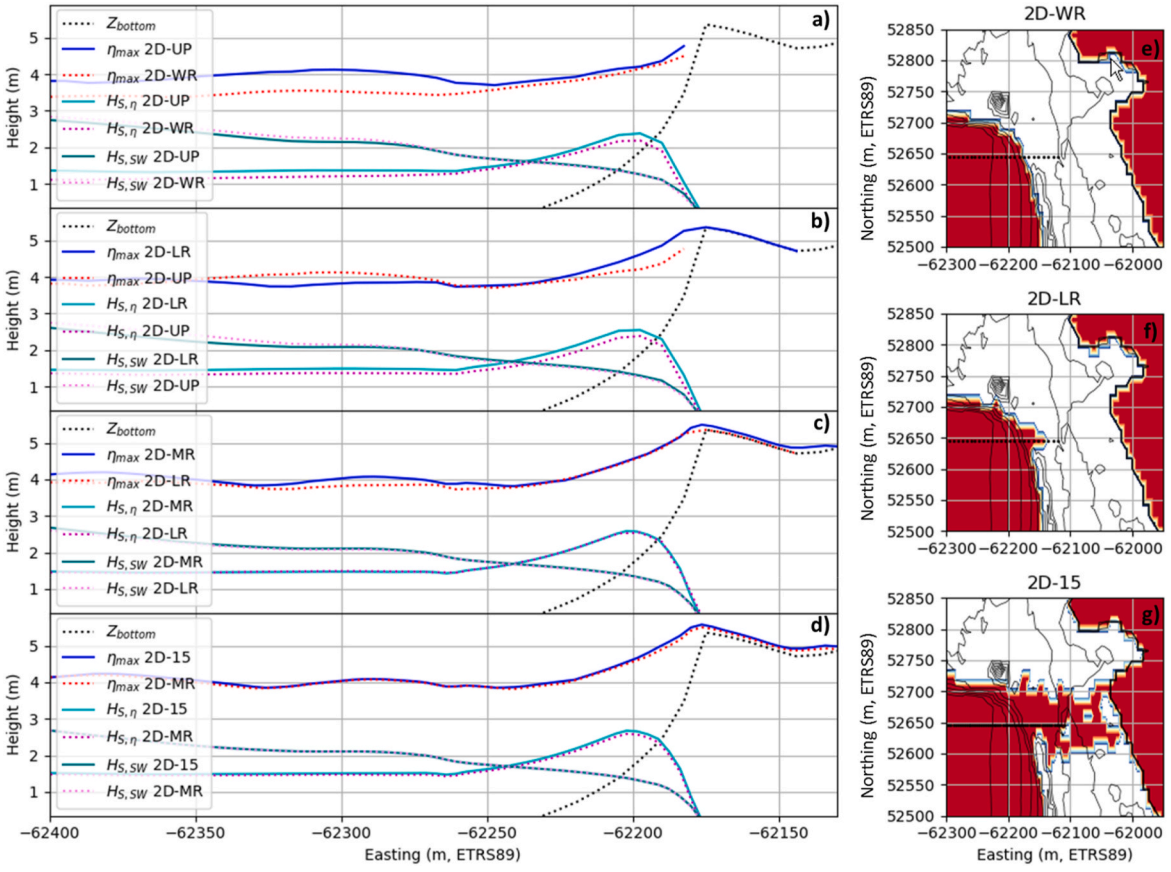

Fig. 13. – a-d) Modelled maximum sea surface elevation (η_{max}), sea surface significant oscillation ($H_{S,\eta}$; **Eq. (11)**) and short-wave significant wave height ($H_{S,SW}$; **Eq. (9)**), for the five 2DH XB-SB configurations listed in Table 1; e-g) overtopping exposure (mapped in red) for the configurations 2D-WR, 2D-LR and 2D-15, the dotted, black cross-shore profiles locate the extraction of the parameters plotted on a-d). Plotted parameters and maps correspond to a single 17-min simulation forced at the offshore boundary with the spectrum shown on Fig. 4 (right panel), and used for maps on Figs. 10 and 11 (right panel).

WR). The calibrated short-wave breaking (2D-LR) further accentuates the differences with 2D-WR, leading to higher $H_{S,\eta}$ (+16.5% at peak) and η_{max} near the shoreline, and ultimately causing an otherwise inexistent overtopping. Assuming that the conclusions of these first two calibration steps, defined for the lower energy forcing in **Section 3**, remain valid for under energetic conditions, they also explain the increase of overtopping exposure from Fig. 13e to f. The differences in η_{max} offshore of the swash zone could be due to the modification to the incident waves by the model setting alone or due to the reflected long waves. However, this issue was not investigated in detail.

5.2.2. Impact of grid resolution and friction

According to the hydrodynamic and topographic data, which were collected under low energy to moderate forcings, the model results were also improved by increasing the cross-shore resolution and by lowering the bottom friction. Indeed, the refined 2D-15 model did compensate for the lack of IG energy over the tidal cycle monitored on 10 March 2020 ((Figs. 6 and 7; see Table B3 for details), while at the same time, it helped producing an almost perfect match between overtopping observations and the modelled exposure maps under the more energetic conditions of 21 February 2019 (Fig. 9). Still, Fig. 12 reveals that, at high tide and under relatively low energy waves, the differences between the coarser model 2D-LR and the refined 2D-15 model are small. Also, under energetic and more saturated conditions, the higher grid resolution of 2D-MR, alone, does not influence the average parameters $H_{S,\eta}$ (+1.2% at peak) and $H_{S,SW}$ significantly (Fig. 13c). However, larger values of η_{max} propagate up to the dune crest. Compared to 2D-LR, the larger η_{max} allows the overtopping discharge to reach further inshore behind the dune crest. The discharge further increases when the bottom friction is reduced (2D-15), driven by slightly higher $H_{S,\eta}$ respectively (+3.5% and +4.7% at peak compared to 2D-MR and 2-LR) and η_{max}. As such, it appears that lowering the bottom friction favours the generation of IG wave under more saturated conditions, like for instance during the lower stage of the tidal cycle used for validation purposes (Fig. 7). Overall, under the saturated conditions tested in **Section 4**, the calibration and refinement of the model increase $H_{S,\eta}$ by 22%, at its peak, from 2D-WR to 2D-15. Combined with a better representation of the wetting-drying in the swash zone offered by the refined grid, this increase certainly explains the contrasting exposure maps that can be modelled with XB-SB (Fig. 13e–f).

5.3. Benefits and limitations of 2DH-surfbeat simulations

Overall, a coarse (2D-LR) and a refined model (2D-MR) were built, respectively capable of running in 11% and 34% of real time. Both models performed similarly in terms of nearshore wave predictions, although the refined model appeared to be more appropriate for mapping the exposure to overtopping. In addition, the refined model was stable with a lower friction coefficient, which provided more accurate IG energy estimates (2D-15). After low and moderate wave conditions were used for validating the model settings, the model's numerical robustness was tested under high energy waves. High energy waves were combined with a rather exceptional tide plus atmospheric surge level so that the approach proved to be robust enough across a wide range of forcing conditions. This combined performance and robustness leaves room to adapt these model settings for near real-time 2DH forecast applications, such as the OPENCoastS service (Oliveira et al., 2021). Depending also on available resources (i.e., speed and number of CPUs), these applications could either be run continuously, similar to what was presented in **Section 3**, or be run to produce inundation maps at specific stages of the tidal cycle, like presented into **Section 5**. Such a forecast would account for the alongshore morphology, as it was initially intended (Fig. 14). Indeed, the plotted fields of average significant wave height for the three wave climates show the wave focusing and shadowing areas produced by the ebb-tidal delta and by the deposited dredged materials in front of the groin fields. In the case of the larger and oblique waves, the northern jetty of the harbour entrance also visibly contributed to some wave shadowing, although this might be exaggerated because diffraction processes are not represented in XB-SB's phase-averaged short-wave solver.

Achieving similar 2DH results with a phase-resolving model would likely increase the numerical requirements by at least an order of magnitude, which explains why most operational applications of phase-resolving solver are likely to remain 1DH (e.g., Henderson et al., 2022; Storlazzi et al., 2022). First, the grid resolution should be significantly increased (see, for instance, de Beer et al., 2021 and da Silva et al., 2022). Then, (unpresented) preliminary tests with the 2DH non-hydrostatic solver of XBeach revealed prohibitive wave shadowing effects at the lateral boundaries. And because of these effects, the present size of the domain turned unworkable and should have been unreasonably increased for the study objectives. So, the alternative of using only 1DH phase-resolving simulation was tested and compared for three cross-shore profiles.

The first comparison, between 1DH and 2D-LR along P1 (Fig. 8a,d), highlighted the overestimation of the IG wave component in the 1DH approach. A similar overestimation was also described by Nicolae Lerma et al. (2017) and Fiedler et al. (2018). The latter authors further highlighted the shortcomings of using theoretical bound wave conditions at

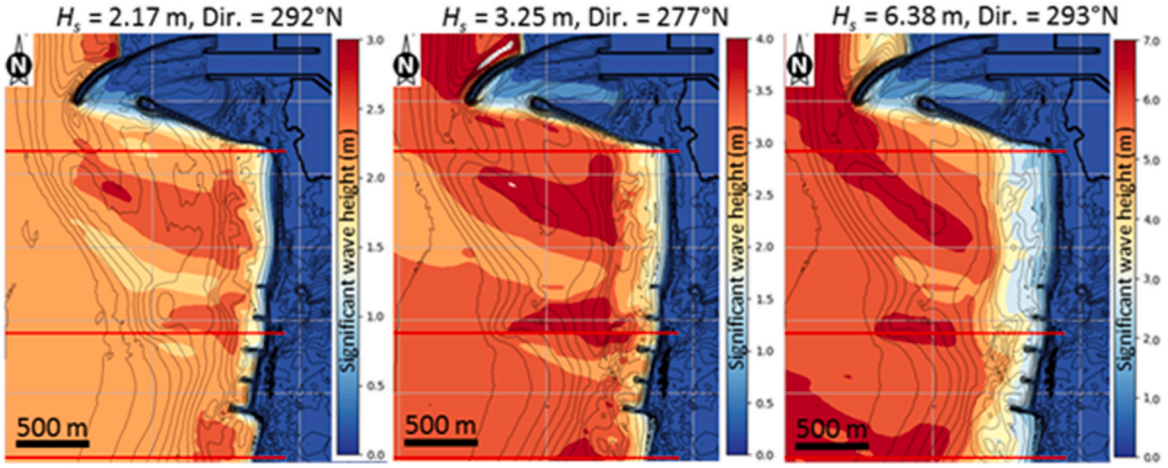

Fig. 14. – Spatial fields of average significant wave height (H_s) corresponding to the simulations presented, from left to right, in Figs. 8a and 11 (left panels), and Fig. 11 (right panels), respectively, for profiles P2, P3 and P1 from on Figure A3 and reproduced in red; nearshore bathymetries are from August 2020 (left panel) and August 2019 (centre and right panels).

the boundary of 1DH models, adding to the strong directional spreading of IG wave, which is not accounted for in 1DH. Likewise, Henderson et al. (2022) found that, with default parameterisation, 1DH non-hydrostatic may overestimate overtopping frequency by a factor of two. Their results were based on overtopping observations at a beach backed with riprap. Also, based on observations, the 2DH surfbeat model in Roelvink et al. (2018) outperformed, in terms of runup, other 1DH and empirical alternatives by seamlessly accounting for the combined effects of the directional spreading and oblique wave incidence. In agreement with these results, comparisons between 1D-NH and 2D-15 along profile P1 and P3 (Fig. 11) suggest that the differences between 1DH phase-resolving and 2DH surfbeat simulations grow with the short-wave angle of incidence and in the vicinity of the harbour entrance.

In summary, on the one hand, several limitations of the 1DH approach can lead to overestimated overtopping rates in areas with alongshore geomorphological complexities. Approaches relying on such models may therefore be very conservative. On the other hand, 2DH surfbeat approaches do not fully represent the short-wave runup, thus underestimating the overtopping rates (Roelvink et al., 2018). Although the use of an unconventional breaking criterion like the one used herein could have balanced this underestimation, a complementary solution may be to resort to nested phase-resolving simulations. The nested simulations could be executed in 1DH or 2DH, with their open boundaries placed in the lee of the wave shadowing and focusing areas. Then, the elevation and velocities at the boundary could be reconstructed, for instance, with an IG wave component from the 2DH surfbeat model and a short-wave component derived from a generic or, preferably, downscaled spectrum. Similar to what Lashley et al. (2020) proposed, another alternative would be to force empirical formulas (e.g., EurOtop 2018) with spectral wave height and period computed with a 2DH surfbeat model. The IG spectrum would be extracted from a 2DH XB-SB model at the shoreline, and combined with a generic spectrum for the short-waves, also based on XB-SB mean parameters. Compared to the methodology of Lashley et al. (2020), no empirical estimates of IG wave parameters are needed, and the computation time remains acceptable for operational uses.

6. Conclusions

To address need for tools to simulate and map the contribution of wind-generated waves to marine flooding hazards, the study presented a workflow to improve a 2DH local inundation model based on a phase-average solver, coupled to a circulation solver. The coupled solvers resolve the sea surface motions up to the surfbeat or infragravity wave timescale (i.e., XBeach in surfbeat mode). The local model settings, namely the short-wave breaking dissipation, the numerical scheme for the short-wave propagation, the cross-shore grid resolution and the bottom friction, were calibrated through cross-validation based on 1) measurements of nearshore waves and 2) the observation of an overtopping event at distinct periods. This calibration was a critical step and largely moulded the predictions of exposure to overtopping as:

- the tuning of the short-wave dissipation (i.e., setting $\delta > 0$) allowed larger wave to reach the shoreline and to overtop the dune crest
- the less diffusive numerical scheme led to larger IG energy and increased inundation extent behind the overtopped dune crest
- refining the cross-shore resolution, as it smoothed the wetting and drying at the shoreline, led to greater inundation behind the dune crest
- reducing the bottom friction coefficient improved the match between modelled and observed nearshore IG energy, enhancing the overtopping discharges

Additionally, forcing the model with appropriate two-dimensional wave spectra, here dynamically downscaled from regional and cross-scale spectral solvers for the generation and propagation wind-waves, was critical for representing wave overtopping. Indeed, when forced with generic spectra (i.e., JONSWAP), with and without accounting for the downscaled wave directional spreading, the model was unable to reproduce the moderate overtopping event used in the calibration.

Despite the calibration, a set of selected simulations further confirmed that the 2DH surfbeat model was less conservative than a 1DH phase-resolving model. However, the inspection of the nearshore elevation spectra and of the spatial fields of the significant wave height highlighted the advantages of the 2DH surfbeat. Namely, in 2DH the surfbeat solvers 1) accounts for directional spreading of short and IG waves and 2) represent the short-wave shadowing - focusing areas created by the morphological features and coastal structures. Under these considerations, the appropriate calibration should allow pushing the 2DH surfbeat solvers at least until the shoreline. Further, for lack of data, it is hard to tell whether they would be more accurate than approaches relying solely on 1DH phase-resolving model or empirical formulas. Instead, the study advocates that, due to its efficiency and robustness, the 2DH XB-SB solver is well suited for mapping the exposure to overtopping where the morphology varies alongshore. For conservativeness, further work is required to assess if such maps should be backed with overtopping discharges computed from the 1DH phase-resolving model and/or empirical formulas. XBeach surfbeat in 2DH should therefore, at least, improve the efficient semi-dynamic approaches developed by, for instance, Gallien (2016), Nicolae Lerma et al., (2018) or Saulnier et al., (2020).

Fundings

This study was initiated and conducted within the scope of the project MOSAIC.pt, funded by the *Fundação para a Ciência e Tecnologia* under the grant number PTDC/CTA-AMB/28909/2017. In addition, XBeach numerical simulations were performed with resources provided by the same institution under the project CPU4MOSAIC+ (CPCA_A1_402953_2021) and SCHISM numerical simulations were performed with resources provided by the Portuguese National Distributed Computing Infrastructure (INCD), funded by Lisboa2020 Operational Program through the INCD project (LISBOA-01-0145-FEDER-022153). For the field work, FCT/MCTES provided financial support to CESAM (UIDP/50017/2020+UIDB/50017/2020), through national funds.

CRediT authorship contribution statement

Alphonse Nahon: Conceptualization, Methodology, Software, Investigation, Formal analysis, Writing - original draft; **André B. Fortunato**: Supervision, Conceptualization, Methodology, Software, Writing - original draft, Project administration, Funding acquisition; **Filipa S·B.F. Oliveira**: Supervision, Conceptualization, Methodology, Software, Writing - original draft; **Alberto Azevedo**: Resources, Software, Writing - Review & Editing; **Maria João Henriques:** Resources, Writing - Review & Editing; **Paulo A. Silva**: Resources, Writing - Review & Editing; **Paulo Baptista**: Resources, Writing - Review & Editing; **Paula Freire**: Resources, Writing - Review & Editing, Project administration, Funding acquisition.

Declaration of competing interest

The authors declare that they have no known competing financial interests or personal relationships that could have appeared to influence the work reported in this paper.

Data availability

Data will be made available on request.

Acknowledgements

The authors warmly acknowledge the developers of WAVEWATCH III®, SCHISM and XBeach, for sharing their code and knowledge with the scientific community. The authors are also grateful to the team of the project MOSAIC.pt, our colleagues from the University of Aveiro and their students for providing valuable help in acquiring the field data, and to our colleague Elsa Alves for providing assistance with the flow data from SNIRH. The SNIRH, the Portuguese Navy (IH) and Portuguese Institute for the Sea and the Atmosphere (IPMA) are acknowledge for providing, respectively, the flow data from the Mondego River, the wave and tide data, and the data from Ferrel's weather station. Lastly, we acknowledge two anonymous reviewers whose comments and suggestions greatly helped to improve the manuscript structure and robustness.

Appendix A. Downscaling workflow and boundary conditions

A.1 Model workflow and atmospheric forcing

Coastal inundation models should account for water level variations driven by wind-waves, tides and atmospheric storm surges (Idier et al., 2019). From a process-based standpoint, this implies to dynamically downscale remote contributions towards the coastal model boundaries. In the present case, the boundary conditions were downscaled using the workflow presented in Oliveira et al. (2021). The workflow includes a North-Atlantic wind-waves model based on WAVEWATCH III® (The WAVEWATCH III® Development Group, 2016; hereafter referred to as WW3), the FES2014 tidal prediction atlas (Lyard et al., 2021), and the cross-scale hydrodynamic solver SCHISM (Zhang et al., 2016). Figure A1 shows where in this workflow the large and cross-scale models are forced with fields of wind and atmospheric pressure over the North-Atlantic basin. This workflow has yielded good results in forecast applications (Oliveira et al., 2021). Here, it was used in hindcast mode for February 2019 and March 2020, forced with the ERA5 reanalysis (Hersbach et al., 2020). The wave model was also run, for comparison purposes, with the first 24-h of daily (i.e., 00 cycle) GFS' atmospheric forecast (NCEP, 2020).

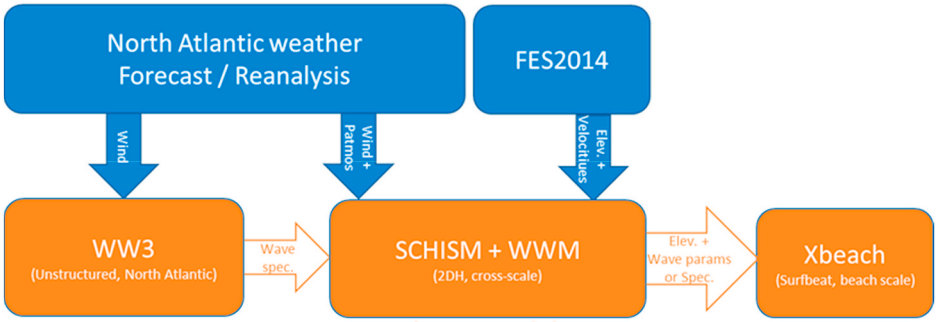

Fig. A.1. - Large scale forcings represented in blue, with the downscaling model workflow represented in orange

A.2 Forcing waves and water levels

A.2.1 Offshore wave climate

Spectral wave conditions at the boundary of the cross-scale model were downscaled with an unstructured wind wave model of the North Atlantic region based on WW3. The model has an unstructured grid extending from 0° to 75°N and from 98°W to 13°E (Figure A2). The grid is composed of ~38 k nodes and ~73 k elements, with a resolution ranging from 0.5° (<56 km) in open ocean areas, to 0.05° (<5.6 km) along the European coast. The model was set up with a spectral discretization of 36 evenly-spaced directions and 36 frequencies ranging from 0.032 Hz to 0.899 Hz with a 1.1 increment factor. Following Alday et al. (2021), the wind fields of the ERA5 reanalysis were used with the T475 parameterization, and after increasing by 5% the wind speeds by over 21 m/s; the simulations forced with the GFS forecasts were performed with the T471 parameterization.

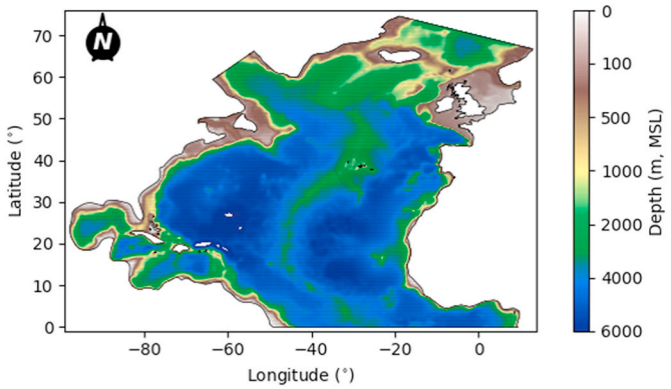

Fig. A.2. Unstructured grid and bathymetry of the North Atlantic wind-wave model

Modelled mean wave parameters were validated against observations at the Leixões buoy, in 83 m water depth (L., Fig. 1a), for the month of

February 2019. Figure A3 and Table A1 summarise the model performance in terms of mean wave parameters. Both simulations underestimate the significant wave height ($H_{S,SW}$) by 5%–7% on average, with an associated root mean square deviation from the observations on the order of 16%–17% of the average $H_{S,SW}$ observed during the 28-day record. The modelled significant wave height maxima peaked at lower values than observations when the observed $H_{S,SW}$ exceeded 5 m. For instance, the observation record during the storm Helena reached 10.5 m on February 1st when both simulations peaked at 9.0 m. So, despite the correction of the stronger winds, the underestimated storm peaks still contribute to the model's overall negative bias in terms of $H_{S,SW}$. In terms of peak periods, the model results matched the buoy data well, and the weighted mean wave directions only presented small biases of two to four degrees: modelled waves were slightly more shore-normal than in the observation record. Overall, these differences are within the range of values presented by Alday et al. (2021), and both simulations performed evenly, although the forecast (GFS) simulation was slightly better. Both simulations were also very similar in terms of directional spreading (DSPR), which was in the range of 7° to 28°. As described in the following sections, both simulations were used. In the case of the overtopping event observed on 21 February 2019, the GFS simulation was preferred because it better reproduced the observed buoy record at that time. For the validation against data from the field campaign of March 2020, the ERA5 simulation was preferred because it yielded slightly better results in terms of infragravity wave energy in the local beach model.

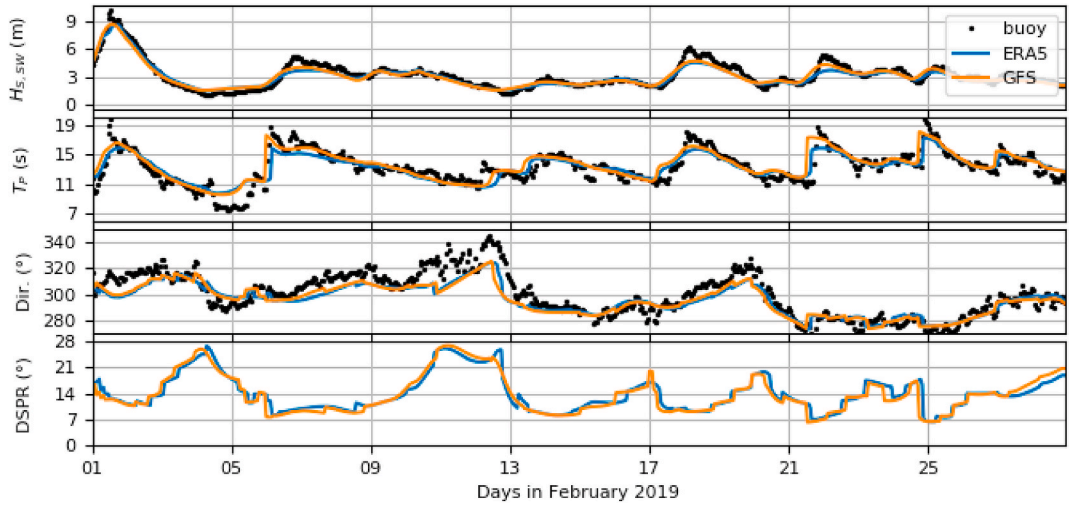

Fig. A.3. Comparison of (3-h filtered) mean wave parameters observed at the Leixões buoy with model results with ERA5 reanalysis and GFS 24-h forecast

Table A.1
- Differences (bias and root mean square, rms, values) between observed and modelled mean wave parameters, in terms of normalised significant wave height ($H_{S,SW}$, in % of the observed mean of 3.25 m), of peak wave period (T_P, in % of the observed mean of 13 s) and of mean wave direction (Dir., weighted average using the observed wave energy estimated from the square of $H_{S,SW}$ times T_P).

Atmospheric forcing	$H_{S,SW}$		T_P		Dir.	
	Bias (%)	RMSD (%)	Bias (%)	RMSD (%)	Bias (°)	RMSD (°)
ERA5	−6.75	17.06	−0.39	10.39	−3.52	11.93
GFS	−5.32	15.69	1.71	10.73	−2.68	10.80

A.2.2 Nearshore waves and water levels

Spectra from the North Atlantic wave model were used as open boundary conditions for a subsequent cross-scale hydrodynamic model. The model is based on SCHISM (Zhang et al., 2016) and covers the coastal region of Figueira da Foz harbour. It extends from 84 m water depth offshore up to 14 km inland along the Mondego River main channel (Figure A4). The SCHISM's phase-average wave solver for wind-wave generation and propagation (WWM; Roland et al., 2012), and its 2DH circulation solver share the same unstructured grid. The grid is composed of ~50 k nodes and ~95 k triangular elements, with a spacing ranging from 2.5 km along the semi-circular open-ocean boundary down to 20 m within the harbour and along the harbour's downdrift shore (i.e., Cova-Gala) and along the river.

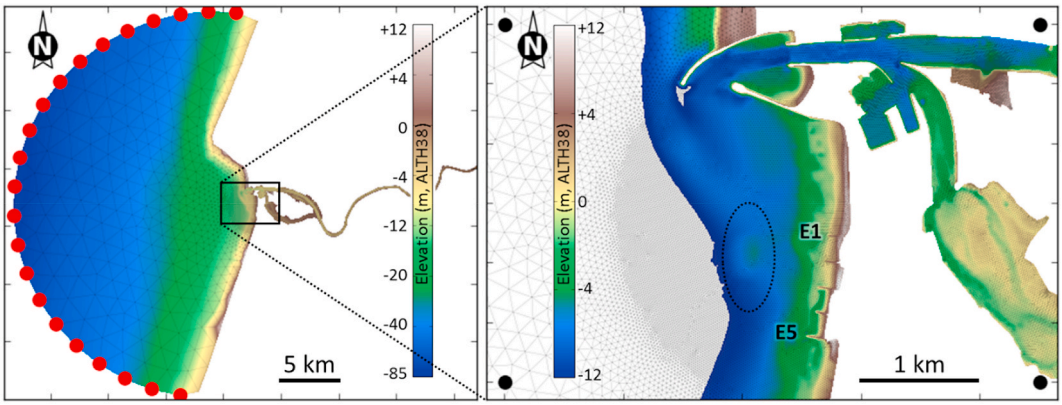

Fig. A.4. - Cross-scale model domain and bathymetry, with SCHISM's 2DH unstructured horizontal grid. On the left panel, red circles stand for the ocean open boundary points where the WW3 spectra and tides plus inverse barometer effect are imposed; on the right panel, the bathymetry up to the −12 m ALTH38 delineates the ebb-tidal delta, and the dotted ellipse indicates the deposition area of dredged materials, E1-5 identify the first and fifth groins indicated on Fig. 1c, and the black circles indicate the XBeach 2DH model's boundary corners

In addition to the WW3 spectra, the open-ocean boundary was forced with tidal elevation and velocities reconstructed with 34 components from FES2014 (Lyard et al., 2021). Tidal water levels were summed to an offshore mean sea level (MSL) that was extrapolated using a quadratic regression fit of monthly mean sea level data from the tidal gauge of Cascais. The tidal gauge record extends since 1882 (Antunes, 2019), giving the study period an MSL of +0.19 m ALTH38 (i.e., Cascais 1938 vertical datum). Atmospheric contributions to the total water level were based on the ERA5 reanalysis. The atmospheric inverse barometer effect and wind forces were also imposed at the ocean boundary and over the computational domain, respectively. Finally, at the Mondego River upstream boundary, observed flow rates at the nearest (about 20 km) upstream station (SNIRH, 2021), were imposed for both February 2019 and March 2020 simulations. Regarding the bathymetry, the offshore and river data were obtained and compiled prior to 2012. Within the area of interest, the shore, the shoreface and the harbour access channel were surveyed either in August 2019, for the February 2019 simulations, or in August 2020, for the March 2020 simulations, in the scope of the national monitoring programme COSMO (COSMonline; https://cosmo.apambiente.pt/).

This cross-scale model was validated against water levels recorded at the tidal gauge located within the harbour (TG, Fig. 1b). In the case of February 2019, available atmospheric pressure measurements from Ferrel meteorological station (F., Fig. 1a) were used to remove the local bias in the reanalysed atmospheric pressure field. Table A2 summarises the differences between modelled and observed elevation, with the +3.9 hPa atmospheric pressure correction in the case of February 2019 and over the high tide-centred 7 h-period during which the pressure sensors gathered hydrodynamic data on 10 March 2020. The comparisons reveal differences of up to 10 cm, which are acceptable given the atmospheric, tidal and steric sea level uncertainties. The enforced good match in February 2019 was important, though as this period was used to validate the overtopping model developed in the next section. Indeed, downscaled water levels and wave spectra were used as boundary conditions at ~15 m water depth in the local models. Unfortunately, no nearshore wave data were available to validate the nearshore wave forcing produced with the cross-scale model. This validation was solely done in the local models.

Table A.2
- Differences (bias and root mean square, rms, values) between observed and modelled elevations at the Figueira da Foz tidal gauge (TG) and between the ERA5 reanalysis and the Ferrel meteorological station.

Period	TG – Elevation –		Ferrel station – Atmos. Press. –
	Bias (cm)	RMSD (cm)	Bias (hPa)
February 2019	−1.3	4.8	+3.9
10 March 2020	10.1	10.7	–

Appendix B. Sensitivity of nearshore short and IG waves to model configurations

The following tables summarize the model's performances, in terms of bias, root mean square differences (Drms), normalised root mean square differences (Ndrms), and/or normalized bias (Nbias) at the level of PT1-3 (Fig. 1) and for the model configurations listed in Table 1. Bias, Nbias and Drms, between observed (obs.) and modelled (mod.) variables, were calculated as follows:

$$\text{Bias} = \frac{1}{N}\sum_{i=1}^{N} mod._i - obs._i$$

$$\text{Nbias} = \frac{1}{N}\sum_{i=1}^{N} \frac{mod._i - obs._i}{obs._i}$$

$$\mathrm{Drms} = \frac{1}{N}\sqrt{\sum_{i=1}^{N}(mod._i - obs._i)^2}$$

$$\mathrm{Ndrms} = \frac{1}{\sum_{i=1}^{N} obs._i}\sqrt{\sum_{i=1}^{N}(mod._i - obs._i)^2}$$

Table B.1
- Bias (cm), Drms (cm) and Ndrms (%) of short-wave significant wave height ($H_{m0,SW}$).

Simulations	$H_{m0,SW}$ PT1			$H_{m0,SW}$ PT2			$H_{m0,SW}$ PT3		
	Bias	Drms	Ndrms	Bias	Drms	Ndrms	Bias	Drms	Ndrms
2D-WR	−3.5	15.6	16.0	1.0	11.0	10.8	5.0	12.3	13.4
2D-UP	−2.8	14.1	14.5	−1.1	11.2	11.0	2.0	12.2	13.2
2D-LR	9.4	13.4	13.8	7.5	11.3	11.1	8.4	13.6	14.8
1D-LR	9.0	11.9	12.2	−2.5	7.8	7.6	−3.4	10.2	11.0
1D-MR	7.9	10.9	11.2	2.4	7.8	7.7	2.3	9.8	10.6
1D-HR	14.0	16.1	16.7	9.8	12.2	12.0	8.1	12.6	13.7
2D-MR	10.5	14.4	14.8	5.0	9.2	9.0	8.6	13.2	14.3
2D-15	11.2	14.0	14.4	5.3	8.9	8.7	9.0	13.0	14.0

Table B.2
Bias (cm) and Nbias (%) of maximum $H_{m0,SW}$ ($H_{max,SW}$).

Simulations	$H_{max,SW}$ PT1		$H_{max,SW}$ PT2		$H_{max,SW}$ PT3	
	Bias	Nbias	Bias	Nbias	Bias	Nbias
2D-WR	−27.3	−18.5	−12.9	−9.4	−5.1	−4.2
2D-UP	−22.1	−14.9	−14.6	−10.6	−8.6	−7.2
2D-LR	−7.1	−4.8	−3.0	−2.16	−0.7	−0.6
1D-LR	−3.0	−2.0	−10.6	−7.7	−10.9	−9.1
1D-MR	−4.7	−3.2	−6.2	−4.5	−4.9	−4.1
1D-HR	0.6	0.4	1.2	0.9	1.9	1.6
2D-MR	−5.4	−3.6	−4.2	−3.1	0.6	0.5
2D-15	−1.1	−0.8	−1.2	−0.9	3.3	2.8

Table B.3
- Bias (cm), Drms (cm) and Ndrms (%) of IG significant wave height ($H_{m0,IG}$).

Simulations	$H_{m0,IG}$ PT1			$H_{m0,IG}$ PT2			$H_{m0,IG}$ PT3		
	Bias	Drms	Ndrms	Bias	Drms	Ndrms	Bias	Drms	Ndrms
2D-WR	−21.3	22.1	36.5	−25.5	26.8	37.4	−20.7	22.5	29.5
2D-UP	−13.0	14.3	23.5	−17.9	19.6	27.4	−9.4	12.9	17.0
2D-LR	−9.7	11.4	18.9	−14.7	17.0	23.7	−5.6	10.2	13.4
1D-LR	6.6	12.0	19.8	11.0	12.9	18.1	2.5	12.6	16.5
1D-MR	7.6	13.0	21.5	−0.2	12.3	17.3	0.0	13.6	17.8
1D-HR	4.6	11.0	18.2	−3.0	11.9	16.7	−3.6	14.3	18.7
2D-MR	−10.7	12.0	19.8	−14.6	17.5	24.5	−10.6	14.3	18.8
2D-15	−2.5	7.5	12.3	6.2	9.9	13.8	−3.2	8.9	11.7

Table B.4
- Performances in terms of spectral IG mean wave period ($T_{m02,IG}$).

Simulations	$T_{m02,IG}$ PT1 (s)		$T_{m02,IG}$ PT2 (s)		$T_{m02,IG}$ PT3 (s)	
	Bias	Drms	Bias	Drms	Bias	Drms
2D-WR	6.5	9.1	2.8	6.3	2.3	4.8
2D-UP	−6.3	8.1	−5.2	8.4	−2.3	4.0
2D-LR	−6.5	8.3	−5.4	8.7	−3.0	4.7
1D-LR	2.9	12.6	4.8	10.3	1.6	5.4
1D-MR	5.0	9.1	4.3	13.0	6.7	8.1
1D-HR	8.1	10.8	5.5	13.6	7.7	9.4
2D-MR	−7.1	8.6	−4.8	8.1	−1.0	3.9
2D-15	−2.7	7.5	−0.3	6.4	3.5	5.6

References

Alday, M., Accensi, M., Ardhuin, F., Dodet, G., 2021. A global wave parameter database for geophysical applications. Part 3: improved forcing and spectral resolution. Ocean Model. 166, 101848 https://doi.org/10.1016/j.ocemod.2021.101848.

Alday, M., Ardhuin, F., Dodet, G., Accensi, M., 2022. Accuracy of numerical wave model results: application to the Atlantic coasts of Europe (preprint). Surface/Numerical Models/Shelf Seas/Surface waves/Other. https://doi.org/10.5194/egusphere-2022-481.

Almar, R., Ranasinghe, R., Bergsma, E.W.J., Diaz, H., Melet, A., Papa, F., Vousdoukas, M., Athanasiou, P., Dada, O., Almeida, L.P., Kestenare, E., 2021. A global analysis of extreme coastal water levels with implications for potential coastal overtopping. Nat. Commun. 12, 3775. https://doi.org/10.1038/s41467-021-24008-9.

Antunes, C., 2019. Assessment of sea level rise at west coast of Portugal mainland and its projection for the 21st century. J. Mar. Sci. Eng. 7, 61. https://doi.org/10.3390/jmse7030061.

Baquerizo, A., Losada, M.A., Smith, J.M., Kobayashi, N., 1997. Cross-shore variation of wave reflection from beaches. J. Waterw. Port, Coast. Ocean Eng. 123, 274–279. https://doi.org/10.1061/(ASCE)0733-950X(1997)123:5(274).

Bertin, X., Olabarrieta, M., 2016. Relevance of infragravity waves in a wave-dominated inlet: IG waves in wave-dominated inlet. J. Geophys. Res. Oceans 121, 5418–5435. https://doi.org/10.1002/2015JC011444.

Bertin, X., de Bakker, A., van Dongeren, A., Coco, G., André, G., Ardhuin, F., Bonneton, P., Bouchette, F., Castelle, B., Crawford, W.C., Davidson, M., Deen, M., Dodet, G., Guérin, T., Inch, K., Leckler, F., McCall, R., Muller, H., Olabarrieta, M., Roelvink, D., Ruessink, G., Sous, D., Stutzmann, É., Tissier, M., 2018. Infragravity waves: from driving mechanisms to impacts. Earth Sci. Rev. 177, 774–799. https://doi.org/10.1016/j.earscirev.2018.01.002.

Bertin, X., Martins, K., Bakker, A., Chataigner, T., Guérin, T., Coulombier, T., Viron, O., 2020. Energy transfers and reflection of infragravity waves at a dissipative beach under storm waves. J. Geophys. Res. Oceans 125. https://doi.org/10.1029/2019JC015714.

Breilh, J.F., Chaumillon, E., Bertin, X., Gravelle, M., 2013. Assessment of static flood modeling techniques: application to contrasting marshes flooded during Xynthia (western France). Nat. Hazards Earth Syst. Sci. 13, 1595–1612. https://doi.org/10.5194/nhess-13-1595-2013.

Chaumillon, E., Bertin, X., Fortunato, A.B., Bajo, M., Schneider, J.-L., Dezileau, L., Walsh, J.P., Michelot, A., Chauveau, E., Créach, A., Hénaff, A., Sauzeau, T., Waeles, B., Gervais, B., Jan, G., Baumann, J., Breilh, J.-F., Pedreros, R., 2017. Storm-induced marine flooding: lessons from a multidisciplinary approach. Earth Sci. Rev. 165, 151–184. https://doi.org/10.1016/j.earscirev.2016.12.005.

COSMonline, n.d. Coastal Monitoring Programme of Continental Portugal - COSMO [WWW Document]. URL https://cosmo.apambiente.pt/ (accessed 5.2.22).

da Silva, R.F., Hansen, J.E., Rijnsdorp, D.P., Lowe, R.J., Buckley, M.L., 2022. The influence of submerged coastal structures on nearshore flows and wave runup. Coast. Eng. 177, 104194 https://doi.org/10.1016/j.coastaleng.2022.104194.

Daly, C., Roelvink, D., van Dongeren, A., van Thiel de Vries, J., McCall, R., 2012. Validation of an advective-deterministic approach to short wave breaking in a surf-beat model. Coast. Eng. 60, 69–83. https://doi.org/10.1016/j.coastaleng.2011.08.001.

de Beer, A.F., McCall, R.T., Long, J.W., Tissier, M.F.S., Reniers, A.J.H.M., 2021. Simulating wave runup on an intermediate–reflective beach using a wave-resolving and a wave-averaged version of XBeach. Coast. Eng. 163, 103788 https://doi.org/10.1016/j.coastaleng.2020.103788.

de Santiago, I., Morichon, D., Abadie, S., Reniers, A.J.H.M., Liria, P., 2017. A comparative study of models to predict storm impact on beaches. Nat. Hazards 87, 843–865. https://doi.org/10.1007/s11069-017-2830-6.

EurOtop, 2018. Manual on wave overtopping of sea defences and related structures. An overtopping manual largely based on European research, but for worldwide application. Van der Meer, J.W., Allsop, N.W.H., Bruce, T., De Rouck, J., Kortenhaus, A., Pullen, T., Schüttrumpf, H., Troch, P. and Zanuttigh, B. www.overtopping-manual.com.

Fernández-Fernández, S., Ferreira, C.C., Silva, P.A., Baptista, P., Romão, S., Fontán-Bouzas, Á., Abreu, T., Bertin, X., 2019. Assessment of dredging scenarios for a tidal inlet in a high-energy coast. J. Mar. Sci. Eng. 7, 395. https://doi.org/10.3390/jmse7110395.

Fiedler, J.W., Smit, P.B., Brodie, K.L., McNinch, J., Guza, R.T., 2018. Numerical modeling of wave runup on steep and mildly sloping natural beaches. Coast. Eng. 131, 106–113. https://doi.org/10.1016/j.coastaleng.2017.09.004.

Fortunato, A.B., Meredith, E.P., Rodrigues, M., Freire, P., Feldmann, H., 2019. Near-future changes in storm surges along the Atlantic Iberian coast. Nat. Hazards 98, 1003–1020. https://doi.org/10.1007/s11069-018-3375-z.

Freire et al, P., 2019. MOSAIC.PT FIELD CAMPAIGNS: Cova-Gala, Vieira and São Pedro de Moel beaches, January-March 2019 (No. 334/2019). LNEC, Lisbon.

Gallien, T.W., 2016. Validated coastal flood modeling at Imperial Beach, California: comparing total water level, empirical and numerical overtopping methodologies. Coast. Eng. 111, 95–104. https://doi.org/10.1016/j.coastaleng.2016.01.014.

Gent, M.R.A. van, 2001. Wave runup on dikes with shallow foreshores. J. Waterw. Port, Coast. Ocean Eng. 127, 254–262. https://doi.org/10.1061/(ASCE)0733-950X(2001)127:5(254).

Guza, R.T., Feddersen, F., 2012. Effect of wave frequency and directional spread on shoreline runup: wave spread effects on runup. Geophys. Res. Lett. 39 https://doi.org/10.1029/2012GL051959 n/a-n/a.

Henderson, C.S., Fiedler, J.W., Merrifield, M.A., Guza, R.T., Young, A.P., 2022. Phase resolving runup and overtopping field validation of SWASH. Coast. Eng., 104128 https://doi.org/10.1016/j.coastaleng.2022.104128.

Hersbach, H., Bell, B., Berrisford, P., Hirahara, S., Horányi, A., Muñoz-Sabater, J., Nicolas, J., Peubey, C., Radu, R., Schepers, D., Simmons, A., Soci, C., Abdalla, S., Abellan, X., Balsamo, G., Bechtold, P., Biavati, G., Bidlot, J., Bonavita, M., Chiara, G., Dahlgren, P., Dee, D., Diamantakis, M., Dragani, R., Flemming, J., Forbes, R., Fuentes, M., Geer, A., Haimberger, L., Healy, S., Hogan, R.J., Hólm, E., Janisková, M., Keeley, S., Laloyaux, P., Lopez, P., Lupu, C., Radnoti, G., Rosnay, P., Rozum, I., Vamborg, F., Villaume, S., Thépaut, J., 2020. The ERA5 global reanalysis. Q. J. R. Meteorol. Soc. 146, 1999–2049. https://doi.org/10.1002/qj.3803.

Holthuijsen, L.H., Booij, N., Herbers, T.H.C., 1989. A prediction model for stationary, short-crested waves in shallow water with ambient currents. Coast. Eng. 13, 23–54. https://doi.org/10.1016/0378-3839(89)90031-8.

Idier, D., Bertin, X., Thompson, P., Pickering, M.D., 2019. Interactions between mean sea level, tide, surge, waves and flooding: mechanisms and contributions to sea level variations at the coast. Surv. Geophys. 40, 1603–1630. https://doi.org/10.1007/s10712-019-09549-5.

Jarrett, J.T., 1976. Tidal Prism - Inlet Area Relationships. U.S. Army Engineer Waterways Experiment Station.

Lashley, C.H., Roelvink, D., van Dongeren, A., Buckley, M.L., Lowe, R.J., 2018. Nonhydrostatic and surfbeat model predictions of extreme wave run-up in fringing reef environments. Coast. Eng. 137, 11–27. https://doi.org/10.1016/j.coastaleng.2018.03.007.

Lashley, C.H., Bertin, X., Roelvink, D., Arnaud, G., 2019. Contribution of infragravity waves to run-up and overwash in the pertuis Breton embayment (France). J. Mar. Sci. Eng. 7, 205. https://doi.org/10.3390/jmse7070205.

Lashley, C.H., Zanuttigh, B., Bricker, J.D., van der Meer, J., Altomare, C., Suzuki, T., Roeber, V., Oosterlo, P., 2020. Benchmarking of numerical models for wave overtopping at dikes with shallow mildly sloping foreshores: accuracy versus speed. Environ. Model. Software 130, 104740. https://doi.org/10.1016/j.envsoft.2020.104740.

Le Roy, S., Pedreros, R., André, C., Paris, F., Lecacheux, S., Marche, F., Vinchon, C., 2015. Coastal flooding of urban areas by overtopping: dynamic modelling application to the Johanna storm (2008) in Gâvres (France). Nat. Hazards Earth Syst. Sci. 15, 2497–2510. https://doi.org/10.5194/nhess-15-2497-2015.

Leijnse, T., van Ormondt, M., Nederhoff, K., van Dongeren, A., 2021. Modeling compound flooding in coastal systems using a computationally efficient reduced-physics solver: including fluvial, pluvial, tidal, wind- and wave-driven processes. Coast. Eng. 163, 103796 https://doi.org/10.1016/j.coastaleng.2020.103796.

Lyard, F.H., Allain, D.J., Cancet, M., Carrère, L., Picot, N., 2021. FES2014 global ocean tide atlas: design and performance. Ocean Sci. 17, 615–649. https://doi.org/10.5194/os-17-615-2021.

Mazzaretto, O.M., Menéndez, M., Lobeto, H., 2022. A global evaluation of the JONSWAP spectra suitability on coastal areas. Ocean Eng. 266, 112756 https://doi.org/10.1016/j.oceaneng.2022.112756.

Mendes, D., Oliveira, T.C.A., 2021. Deep-water spectral wave steepness offshore mainland Portugal. Ocean Eng. 236, 109548 https://doi.org/10.1016/j.oceaneng.2021.109548.

Mendes, J., Ruela, R., Picado, A., Pinheiro, J.P., Ribeiro, A.S., Pereira, H., Dias, J.M., 2021. Modeling dynamic processes of Mondego estuary and óbidos lagoon using Delft3D. J. Mar. Sci. Eng. 9, 91. https://doi.org/10.3390/jmse9010091.

Mouragues, A., Bonneton, P., Lannes, D., Castelle, B., Marieu, V., 2019. Field data-based evaluation of methods for recovering surface wave elevation from pressure measurements. Coast. Eng. 150, 147–159. https://doi.org/10.1016/j.coastaleng.2019.04.006.

Mouragues, A., Bonneton, P., Castelle, B., Martins, K., 2021. Headland rip modelling at a natural beach under high-energy wave conditions. J. Mar. Sci. Eng. 9, 1161. https://doi.org/10.3390/jmse9111161.

Nahon, A., et al., 2020. MOSAIC.PT FIELD CAMPAIGNS: Cova-Gala Beach, March 2020 (No. 347/2020). LNEC, Lisbon.

NCEP, 2020. Global Forecast System [WWW Document]. Natl. Cent. Environ. Inf. NCEI. URL. http://www.ncei.noaa.gov/products/weather-climate-models/global-forecast, 3.15.22.

Nicolae Lerma, A., Pedreros, R., Robinet, A., Sénéchal, N., 2017. Simulating wave setup and runup during storm conditions on a complex barred beach. Coast. Eng. 123, 29–41. https://doi.org/10.1016/j.coastaleng.2017.01.011.

Nicolae Lerma, A., Bulteau, T., Elineau, S., Paris, F., Durand, P., Anselme, B., Pedreros, R., 2018. High-resolution marine flood modelling coupling overflow and overtopping processes: framing the hazard based on historical and statistical approaches. Nat. Hazards Earth Syst. Sci. 18, 207–229. https://doi.org/10.5194/nhess-18-207-2018.

Oliveira, J.N.C., 2016. Modelling the Impact of the Extension of the North Jetty of the Mondego River Inlet on the Adjacent Southern Beaches (MSc). Instituto Superior Técnico, Portugal.

Oliveira, J.N.C., 2022. Beach Morphodynamics Modelling for the Improvement of Coastal Protection Solutions. (PhD). Instituto Superior Técnico, Portugal.

Oliveira, J.N.C., Oliveira, F.S.B.F., Trigo-Teixeira, A.A., 2016. Coastline evolution south of the Mondego river inlet: modelling the impact of the extension of the north jetty. In: Proceedings of the 4th Hydrographic Engineering Conference. Hydrographic Institute, Portugal, pp. 245–248.

Oliveira, T.C.A., Neves, M.G., Fidalgo, R., Esteves, R., 2018. Variability of wave parameters and Hmax/Hs relationship under storm conditions offshore the Portuguese continental coast. Ocean Eng. 153, 10–22. https://doi.org/10.1016/j.oceaneng.2018.01.080.

Oliveira, A., Fortunato, A.B., Rodrigues, M., Azevedo, A., Rogeiro, J., Bernardo, S., Lavaud, L., Bertin, X., Nahon, A., de Jesus, G., Rocha, M., Lopes, P., 2021. Forecasting contrasting coastal and estuarine hydrodynamics with OPENCoastS. Environ. Model. Software 143, 105132. https://doi.org/10.1016/j.envsoft.2021.105132.

Quataert, E., Storlazzi, C., van Dongeren, A., McCall, R., 2020. The importance of explicitly modelling sea-swell waves for runup on reef-lined coasts. Coast. Eng. 160, 103704 https://doi.org/10.1016/j.coastaleng.2020.103704.

Raubenheimer, B., Guza, R.T., 1996. Observations and predictions of run-up. J. Geophys. Res. Oceans 101, 25575–25587. https://doi.org/10.1029/96JC02432.

Rebêlo, L., Nave, S.O., 2022. Long-term Coastline evolution of Figueira da Foz – nazaré sector (Portugal). Rev. Gest. Costeira Integrada 22, 145–168. https://doi.org/10.5894/rgci-n507.

Roelvink, J.A., 1993. Dissipation in random wave groups incident on a beach. Coast. Eng. 19, 127–150. https://doi.org/10.1016/0378-3839(93)90021-Y.

Roelvink, D., Reniers, A., van Dongeren, A., van Thiel de Vries, J., McCall, R., Lescinski, J., 2009. Modelling storm impacts on beaches, dunes and barrier islands. Coast. Eng. 56, 1133–1152. https://doi.org/10.1016/j.coastaleng.2009.08.006.

Roelvink, D., McCall, R., Mehvar, S., Nederhoff, K., Dastgheib, A., 2018. Improving predictions of swash dynamics in XBeach: the role of groupiness and incident-band runup. Coast. Eng. 134, 103–123. https://doi.org/10.1016/j.coastaleng.2017.07.004.

Roland, A., Zhang, Y.J., Wang, H.V., Meng, Y., Teng, Y.-C., Maderich, V., Brovchenko, I., Dutour-Sikiric, M., Zanke, U., 2012. A fully coupled 3D wave-current interaction model on unstructured grids: 3D wave-current model. J. Geophys. Res. Oceans 117. https://doi.org/10.1029/2012JC007952 n/a-n/a.

Saulnier, J.-B., Paquereau–Gaboreau, T., Delemasure, J.-V., 2020. Implementation of overtopping discharges in a 2D coastal flood model of the Mont Saint-Michel Bay. In: Presented at the 2020 TELEMAC User Conference, Antwerp, Belgium, pp. 73–80.

Smit, P., Zijlema, M., Stelling, G., 2013. Depth-induced wave breaking in a non-hydrostatic, near-shore wave model. Coast. Eng. 76, 1–16. https://doi.org/10.1016/j.coastaleng.2013.01.008.

Smith, J.M., Larson, M., Kraus, N.C., 1993. Longshore current on a barred beach: field measurements and calculation. J. Geophys. Res. 98, 22717 https://doi.org/10.1029/93JC02116.

Smith, R.A.E., Bates, P.D., Hayes, C., 2012. Evaluation of a coastal flood inundation model using hard and soft data. Environ. Model. Software 30, 35–46. https://doi.org/10.1016/j.envsoft.2011.11.008.

SNIRH, 2021. Daily average river flow measured between November 2005 and October 2021 (87% temporal coverage) at Açude Ponte Coimbra station from the Sistema Nacional de Informação de Recursos Hídricos [WWW Document]. URL. https://snirh.apambiente.pt/, 8.28.2022.

Stockdon, H.F., Thompson, D.M., Plant, N.G., Long, J.W., 2014. Evaluation of wave runup predictions from numerical and parametric models. Coast. Eng. 92, 1–11. https://doi.org/10.1016/j.coastaleng.2014.06.004.

Storlazzi, C.D., Rey, A.E., van Dongeren, A.R., 2022. A numerical study of geomorphic and oceanographic controls on wave-driven runup on fringing reefs with shore-normal channels. J. Mar. Sci. Eng. 10, 828. https://doi.org/10.3390/jmse10060828.

The WAVEWATCH III® Development Group, 2016. User Manual and System Documentation of WAVEWATCH III® Version 5.16 (Tech. Note No. 329). NOAA/NWS/NCEP/MMAB, College Park, MD, USA.

Van Dongeren, A., Reniers, A., Battjes, J., Svendsen, I., 2003. Numerical modeling of infragravity wave response during DELILAH. J. Geophys. Res. 108, 3288. https://doi.org/10.1029/2002JC001332.

van Ormondt, M., Roelvink, D., van Dongeren, A., 2021. A model-derived empirical formulation for wave run-up on naturally sloping beaches. J. Mar. Sci. Eng. 9, 1185. https://doi.org/10.3390/jmse9111185.

Vitousek, S., Barnard, P.L., Fletcher, C.H., Frazer, N., Erikson, L., Storlazzi, C.D., 2017. Doubling of coastal flooding frequency within decades due to sea-level rise. Sci. Rep. 7, 1399. https://doi.org/10.1038/s41598-017-01362-7.

Vousdoukas, M.I., Voukouvalas, E., Mentaschi, L., Dottori, F., Giardino, A., Bouziotas, D., Bianchi, A., Salamon, P., Feyen, L., 2016. Developments in large-scale coastal flood hazard mapping. Nat. Hazards Earth Syst. Sci. 16, 1841–1853. https://doi.org/10.5194/nhess-16-1841-2016.

Zhang, Y.J., Ye, F., Stanev, E.V., Grashorn, S., 2016. Seamless cross-scale modeling with SCHISM. Ocean Model. 102, 64–81. https://doi.org/10.1016/j.ocemod.2016.05.002.